Modification of inertial oscillations by the mesoscale eddy field

Shane Elipot,[1] Rick Lumpkin,[2] and Germán Prieto[3]

Received 31 July 2009; revised 13 May 2010; accepted 25 May 2010; published 14 September 2010.

[1] The modification of near-surface near-inertial oscillations (NIOs) by the geostrophic vorticity is studied globally from an observational standpoint. Surface drifter are used to estimate NIO characteristics. Despite its spatial resolution limits, altimetry is used to estimate the geostrophic vorticity. Three characteristics of NIOs are considered: the relative frequency shift with respect to the local inertial frequency; the near-inertial variance; and the inverse excess bandwidth, which is interpreted as a decay time scale. The geostrophic mesoscale flow shifts the frequency of NIOs by approximately half its vorticity. Equatorward of 30°N and S, this effect is added to a global pattern of blue shift of NIOs. While the global pattern of near-inertial variance is interpretable in terms of wind forcing, it is also observed that the geostrophic vorticity organizes the near-inertial variance; it is maximum for near zero values of the Laplacian of the vorticity and decreases for nonzero values, albeit not as much for positive as for negative values. Because the Laplacian of vorticity and vorticity are anticorrelated in the altimeter data set, overall, more near-inertial variance is found in anticyclonic vorticity regions than in cyclonic regions. While this is compatible with anticyclones trapping NIOs, the organization of near-inertial variance by the Laplacian of vorticity is also in very good agreement with previous theoretical and numerical predictions. The inverse bandwidth is a decreasing function of the gradient of vorticity, which acts like the gradient of planetary vorticity to increase the decay of NIOs from the ocean surface. Because the altimetry data set captures the largest vorticity gradients in energetic mesoscale regions, it is also observed that NIOs decay faster in large geostrophic eddy kinetic energy regions.

Citation: Elipot, S., R. Lumpkin, and G. Prieto (2010), Modification of inertial oscillations by the mesoscale eddy field, *J. Geophys. Res.*, *115*, C09010, doi:10.1029/2009JC005679.

1. Introduction

[2] It is crucial to understand the dynamics and temporal evolution of near-inertial oscillations (NIOs) for the energy budget of the ocean. NIOs are generated near the surface, predominantly by the wind, propagate in the horizontal and vertical directions and eventually dissipate and contribute to ocean mixing. Propagation from the region of generation is associated with wave refraction, change of frequency or phase, and vertical modes separation. Thus, a relevant metric to characterize the evolution of NIOs is the time scale over which these vertical modes separate, or become out of phase with an originally purely inertially rotating wave [*Gill*, 1984].

[3] The linear theory of *Gill* [1984] predicts that the gradient of planetary vorticity (β) contributes to modes separation. However, discrepancies between this theory [*D'Asaro*, 1995] and oceanic observations suggest other mechanisms, such as the modification of NIOs by the subinertial geostrophic flow, or more generally the interaction between the two. The goal of this paper is to report on global observations of NIO characteristics related to their refraction, magnitude and time evolution, and to relate these to the geostrophic flow, notably its vorticity.

[4] A key element in the theory related to these interactions is the separation (or not) of spatial scales between NIOs and the geostrophic flow. *Kunze* [1985] examined the propagation of NIOs or waves in a geostrophic shear with similar horizontal scales. In this case, in the dispersion relation for the intrinsic frequency of a plane wave, the inertial frequency f is replaced by an effective inertial frequency $f_{\mathrm{eff}} = f + \zeta/2$ where ζ is the vorticity arising from the geostrophic flow. Using a ray path approach, *Kunze* [1985] predicted near-inertial wave trapping in regions of negative (anticyclonic) vorticity in a barotropic jet, and trapping and amplification in a baroclinic jet. Note that these predictions are applicable when NIOs are generated *inside* the vorticity region, so that the effective frequency is also the intrinsic frequency of the NIOs. A number of observational studies have supported this prediction [e.g., *Kunze and Sanford*, 1984; *Poulain et al.*, 1992; *Rainville and Pinkel*, 2004].

[5] *Young and Ben Jelloul* [1997] studied the theoretical evolution of NIOs in a geostrophic field of eddies with spatial

[1]National Oceanography Centre, Liverpool, UK.
[2]NOAA Atlantic Oceanographic and Meteorological Laboratory, Miami, Florida, USA.
[3]Departamento de Física, Universidad de los Andes, Bogota, Colombia.

0148-0227/10/2009JC005679

scales smaller than NIOs, and predicted that the structure of NIOs should be proportional to the eddy stream function. They also noted that the stream function was negatively correlated with the vorticity and hence also predicted constructive interference of NIOs in regions of anticyclonic ζ. *Klein and Llewellyn-Smith* [2001] studied the horizontal dispersion of NIOs in a mesoscale eddy field, decomposing geostrophic and inertial motions in vertical modes. Their analyses revealed that for each NIO vertical mode there should exist a critical horizontal wave number that separates two regimes: one for which large-scale NIO structures are trapped and one where small-scale NIO structures are strongly dispersed. *Klein et al.* [2004b] showed by analytical and numerical methods that under some specific conditions of the vorticity field (vorticity spectrum with a slope shallower than −4), the NIO kinetic energy field should resemble the Laplacian of the vorticity $\nabla^2\zeta$. *Danioux et al.* [2008] studied analytically and numerically the vertical propagation of wind energy, and showed that the correlation between NIO energy and $\nabla^2\zeta$ is a function of the wave number of the eddy field. They also showed that a shallow maximum of near-inertial vertical kinetic energy was related to the gradient of vorticity $\nabla\zeta$. From the study of drifters released during the STORM experiment as well as numerical simulations, *van Meurs* [1998] concluded that $\nabla\zeta$, acting like β, should be considered for the interaction between NIOs and the geostrophic flow when their spatial scales are similar, in order to explain the decay of NIO energy. *Polzin* [2008] revisited vertical profiles of horizontal velocity from the Mid-Ocean Dynamics Experiment and argued that they were representative of a "wave capture" scenario [*Bühler and McIntyre*, 2005], where the characteristics of a near-inertial wave packet are determined by the Doppler shifting of the intrinsic frequency by the background flow, through its horizontal strain and vertical shear. Recently, *Park et al.* [2009] used the global drifter data set to show how the characteristics of NIOs are conditioned by wind stress forcing and near-surface oceanic stratification, but did not consider the influence of the geostrophic flow.

[6] In this paper, we study from a global observational standpoint the influence of the geostrophic vorticity field on NIOs, and attempt to interpret these observations in the various theoretical frameworks presented above. Relevant characteristics of NIOs can be conveniently described in the frequency domain. In oceanic velocity frequency power spectra, the inertial peak is ubiquitous, and is clearly seen in surface drifter data [e.g., *Poulain et al.*, 1992; *Elipot and Lumpkin*, 2008]. The frequency of the peak and its difference from the local inertial frequency can indicate the refraction of NIOs. *Fu* [1981] states that the inertial peak bandwidth is inversely proportional to the "persistence" of inertial waves, which is a time scale that can be related to their decay (see section 3). The integral of the inertial peak is representative of near-inertial variance, and hence of the magnitude of the oscillation or wave. *Elipot and Lumpkin* [2008] showed that a high temporal resolution data set from the Global Drifter Program (GDP) can be used to estimate inertial variance on a global scale [see also *Chaigneau et al.*, 2008]. In this study we use the same data set, described in section 2. Using spectral methods described in section 3, we report in section 4 some global characteristics of NIOs. Then, the modification of near-surface NIOs by the mesoscale is studied by combining sea surface height data from altimetry in section 5. We conclude with a discussion and summary in section 6.

2. Data

[7] NIO characteristics are derived using data from the GDP (http://www.aoml.noaa.gov/phod/dac/gdp.html) from January 2000 to December 2007. The basic data set are the quality-controlled [*Lumpkin and Pazos*, 2007] drifter positions before kriging interpolation [*Hansen and Poulain*, 1996] to quarter day values. Processing of the data is documented by *Elipot and Lumpkin* [2008]; in summary, a single drifter trajectory is considered uninterrupted if no time interval between two successive positions is greater than 6 h. From spline-interpolated hourly positions, hourly drifter velocities are computed by a 2 h centered difference. This high-resolution data set has become considerably larger since January 2005, when the tracking of GDP drifters switched from a service of two satellites to at least five satellites [*Elipot and Lumpkin*, 2008]. *Elipot and Lumpkin* [2008] showed that this data set allows global resolution of inertial and tidal oscillations.

[8] Archiving, Validation and Interpretation of Satellite Oceanographic (AVISO) sea surface height anomaly (SSHA) weekly delayed mode gridded maps [*Ducet et al.*, 2000] were used to estimate geostrophic velocity anomaly fields at the surface. These maps are available on a 1/3° Mercator grid leading to an approximate 36.6 km resolution at the equator down to 5.1 km at 88°N or S. These anomalies were augmented by a mean geostrophic velocity derived from the 0.5° resolution mean dynamic topographic of *Rio and Hernandez* [2004] to obtain the total geostrophic velocity field. From these, the eddy kinetic energy was computed and the vorticity, its gradient and its Laplacian were obtained by differentiating successively in the zonal and meridional directions. Each of these quantities were interpolated in space and time to all hourly drifter locations, and their average values were computed for a trajectory segment of a given length (here 20 days, see section 3). We did not consider data located within 10° of the equator, to avoid problems with geostrophy there. As a consequence, the longest near-inertial period considered is approximately 2.9 days. Consequently, we compare the "fast" evolving NIOs against properties of the relatively slow geostrophic flow. Regions in which the characteristics of the geostrophic flow could not be estimated due to a lack of altimetry data, typically close to the coasts, were not examined in this study.

[9] Figure 1 shows the the number of hourly drifter velocity observations in 1° bins retained for this study (the criteria used to retain data are also defined by our methodology and described in section 3).

3. Methods

[10] Typical Lagrangian time scales estimated from drifter data are 2–3 days [e.g., *Lumpkin et al.*, 2002; *Zhurbas and Oh*, 2003]. Thus, drifter trajectories divided here in 20 day nonoverlapping segments are considered independent realizations. Velocity frequency spectra were computed for each of them. The original number of drifter segments was large (over 30,000), requiring automated procedures to analyze these data.

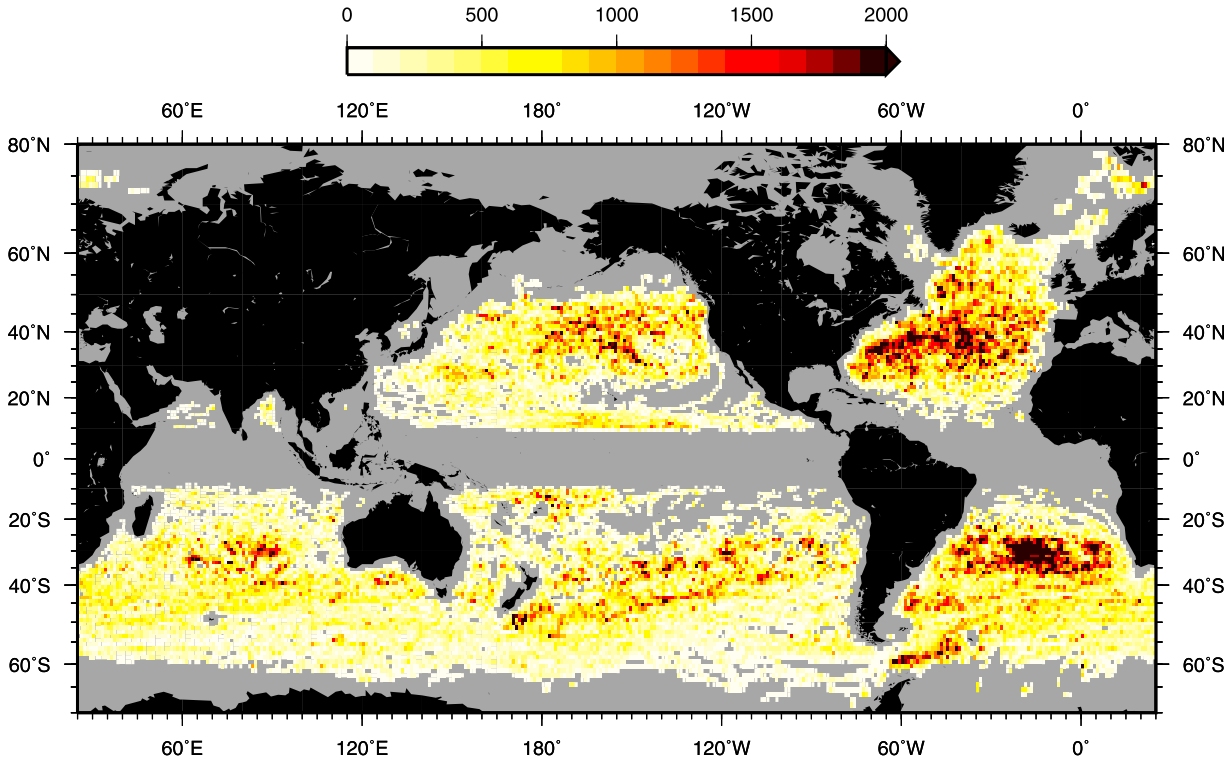

Figure 1. Number of hourly velocity observations in 1° bins. Gray indicates absence of data or areas were no data were selected for the analysis.

3.1. Spectral Estimates

[11] Pseudo-Eulerian velocity spectra were estimated by the quadratic multitaper method of *Prieto et al.* [2007] which expands on the adaptive method of *Thomson* [1982] and proves to be superior for our purpose. Examples of spectral estimates are shown in Figure 2 for real drifter data and for a monochromatic synthetic signal. Details about the quadratic method are given by *Prieto et al.* [2007]. In this study, we used 6 tapers for a time-bandwidth product of 4.

3.2. Relative Frequency Shift, Inverse Excess Bandwidth, and Near-Inertial Variance

[12] The spectrum of a vector time series decomposes the variance in counter-rotating circular components [e.g., *Gonella*, 1972], with positive (negative) frequencies corresponding to counterclockwise (clockwise) rotating motions, cyclonic (anticyclonic) in the Northern Hemisphere. Thus, f is the cyclonic Coriolis frequency, and $-f$ is the anticylonic inertial frequency.

[13] The near-inertial peak of each spectrum was identified as the maximum closest to $-f$ set by the mean latitude of the corresponding 20 day trajectory. Cases for which $-f$ or the diagnosed inertial peak frequency were within the zero-frequency band were discarded. Trajectory segments with their mean positions within 10° of the equator were also discarded because of the ambiguity in distinguishing NIOs from other low-frequency motions. The frequency shift Δf is the difference between the frequency of the diagnosed peak and $-f$. The relative frequency shift (RFS) is defined as

$$\mathrm{RFS} = \frac{\Delta f}{f}. \tag{1}$$

A positive RFS means that NIOs have a frequency of oscillation higher than the local inertial frequency and are shifted cyclonically. In the example of Figure 2, the RFS is −0.034.

[14] A local maximum always exists in a spectrum computed from real world data, due to noise in the absence of true NIOs. In order to make sure that the peak was significant, we looked for "cutoff" frequencies at half power of the peak [*Fu*, 1981; *van Haren*, 2004; *Alford and Whitmont*, 2007], in ranges extending to the next spectrum minima on both sides of the peak (an example is given in Figure 2c). If such cutoffs were not found then the segment was discarded from the analysis. A bandwidth $\Delta\nu > 0$ for the near-inertial peak is defined as the difference between the two cutoff frequencies. For a time series consisting of a single monochromatic velocity oscillation, the theoretical spectrum is a Dirac function at the frequency of the oscillation with a null bandwidth. For the spectral estimate implemented here, the minimum bandwidth $\Delta\nu_r$ is the time-bandwidth product (4) times the spectral resolution $1/T$ (T = 20 days), that is, 0.2 cycles per day (cpd). We therefore define the excess bandwidth as $\Delta\nu - \Delta\nu_r$. Rather than considering the excess bandwidth, we consider the inverse excess bandwidth (IEB)

$$\mathrm{IEB} = \frac{1}{\Delta\nu - \Delta\nu_r}. \tag{2}$$

IEB has units of time, and is interpreted as a measure of the time scale of NIOs. *Fu* [1981] states that the inverse of the bandwidth is a measure of the persistence time scale of a quasiperiodic motion. Similarly, *van Haren* [2004] discusses an "intermittency factor" which corresponds to $|f|/\Delta\nu$. In Figure 2, the IEB is 16.3 days.

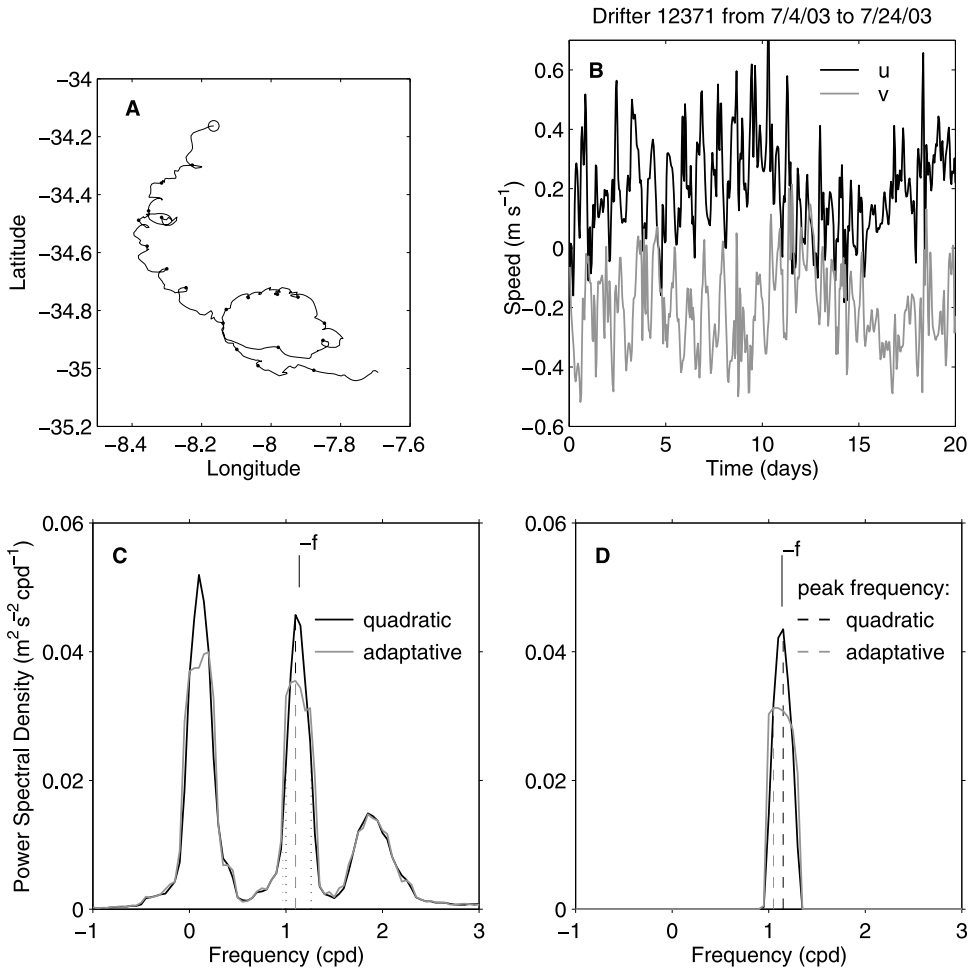

Figure 2. (a) Trajectory of drifter 12371 (Atlantic Oceanographic and Meteorological Laboratory (AOML) identification number) from 4 July 2003 to 24 July 2003. The circle indicates the drifter position at the beginning of the time series. Black dots along the trajectory are plotted every 24 h. (b) Zonal (u, black, offset by 0.1 m s^{-1}) and meridional (v, gray, offset by −0.1 m s^{-1}) velocity components computed over 2 h windows for this trajectory. (c) Drifter velocity spectral estimates by the quadratic (QM) and adaptive (AM) methods. The black dashed line indicates the inertial frequency diagnosed for the QM estimate and the gray dashed line for the AM estimate. The black dotted lines indicate the cutoff frequencies for the quadratic estimate while the gray dotted line indicates a single cutoff frequency found for the adaptive estimate. A secondary shoulder peak appears on the right of the peak for the adaptive estimate that prevents an upper frequency cutoff to be found (see section 3). Here $-f$ denotes the mean inertial frequency for this trajectory segment. (d) Spectral estimates for a synthetic signal constituted of a single circular oscillation at the expected inertial frequency of drifter 12371. The black dashed line indicates the diagnosed peak frequency for the QM estimate. The gray dashed line is the AM estimate.

[15] To help interpret the IEB, a simple but plausible case is presented in Figure 3 which relates IEB to an exponential decay time scale for a velocity oscillation. Figure 3a shows the idealized case of a periodic velocity oscillation starting at the median time of the time series, which is attenuated exponentially. Figure 3b is the corresponding spectrum. Figure 3c shows how the diagnosed IEB varies as a function of the exponential time scale and the oscillation frequency. In such idealized cases, the interpretation of IEB as a time scale of evolution is independent of the mean latitude of the drifter time series. We emphasize that this direct relationship is empirical in the sense that it is only applicable to our methods; the absolute value of the IEB of a peak depends on the parameters used for the spectral estimate. Nevertheless, the relative variations of IEB with respect to other characteristics of the flow or environmental conditions still provide relevant information. For the remainder of this study, we interpret IEB as a measure of the time scale of NIOs: smaller values of IEB correspond to relatively faster evolution of NIOs.

[16] Next, we define the near-inertial variance (NIV) of NIOs as the integral of the spectrum between the two cutoff frequencies of the inertial peak, i.e.,

$$\mathrm{NIV} = \int_{\Delta\nu} S(\nu)\, d\nu. \tag{3}$$

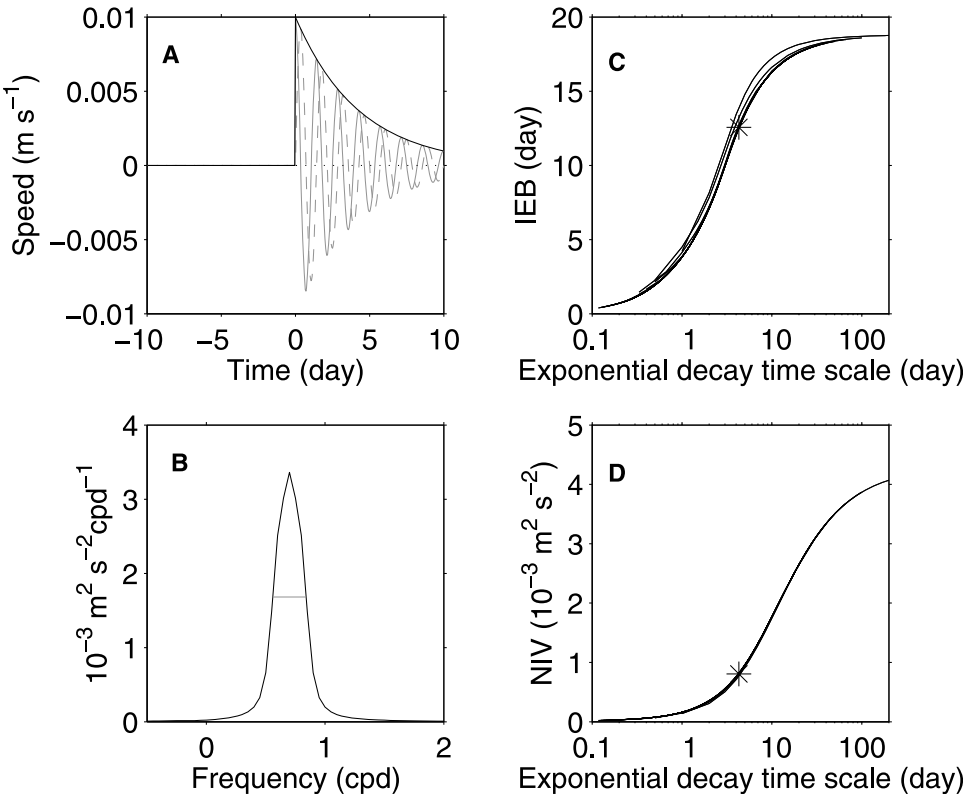

Figure 3. (a) The 20 day time series of the zonal and meridional components of a monochromatic velocity time series written in the complex form $\mathbf{u}(t) = 0$ for $t < 0$ and $\mathbf{u}(t) = 0.01 \exp[i(2\pi\nu t) - t/r]$ for $t > 0$. Here $\nu = 0.7$ cpd, $T = 20$ days and $r = 3$ days. (b) Power spectral density estimate for **u**. The gray horizontal line shows the half power bandwidth of the peak. (c) The asterisk shows the value of the inverse excess bandwidth of the spectrum in Figure 3b and the corresponding exponential decay time scale r of the original time series shown in Figure 3a. The curves show the empirical relationship obtained when ν is varied between ±0.1 and ±1.7 cpd at 0.1 cpd interval, and r is varied between 0.1 and 20 times the oscillation period $1/\nu$. All the curves approximately fall under one curve and are almost indistinguishable, showing that IEB is independent of the frequency of inertial oscillation and hence latitude for its interpretation. (d) The asterisk shows the value of the near-inertial variance deduced from the spectrum in Figure 3b. The curves show the empirical relationships when ν and r are varied as in Figure 3c.

This is the kinetic energy of the near-inertial peak [*Alford and Whitmont*, 2007]. For a monochromatic velocity oscillation, NIV is approximately the total variance of the time series and its square root is the amplitude of the velocity. Figure 2 shows the case of (real) NIOs in a time series that also includes lower- and higher-frequency variations. For this example, the computed total variance is 0.0473 m^2 s^{-2} while the variance contained in the inertial peak is 0.0102 m^2 s^{-2}.

[17] NIV is a measure of variance within a 20 day drifter trajectory. If the inertial oscillation is damped, less variance is captured (see Figure 3d for the idealized case described above). As a consequence, both the amplitude and the width of the inertial peak enter the computation of NIV. In general, NIV will grow with IEB (Figures 3c and 3d). However, we will see that these two parameters do not always exhibit a systematic relationship as external parameters such as the characteristics of the geostrophic flow influence them differently.

3.3. Removing the Tidal Signals

[18] Tidal peaks at near-diurnal and semidiurnal frequencies are present in this data set, as shown by *Elipot and Lumpkin* [2008], and could potentially be misidentified as inertial peaks shifted in frequency. To minimize this diagnostic error, we subtracted from each drifter velocity measurement an estimate of the barotropic tidal velocity. The Oregon State University Topex/Poseidon global inverse solution version 7.1 [*Egbert and Erofeeva*, 2002] was used to estimate the velocity arising from the first eight major tidal constituents (Q1, O1, P1, K1, N2, M2, S2, K2). Figure 4b shows an example where a shifted inertial peak was detected in the spectrum of the original time series, whereas in the spectrum of the detided time series, no inertial peak was detected.

[19] In other cases, significant peaks still remained within the diurnal or semidiurnal bands and their exact nature remained unclear (e.g., Figure 4a). In such cases, we speculate that the actual barotropic signal could be underestimated by the inverse model, or that a baroclinic tidal velocity existed in the data. This occurred mainly for near-semidiurnal peaks in the North Atlantic north of 60°N and in the Southern Ocean east of Drake Passage and around Macquarie Ridge south of New Zealand, where large-amplitude and large-wavelength M2 baroclinic internal tides are predicted by global baroclinic tidal models [*Simmons et al.*, 2004]. Nevertheless, it could

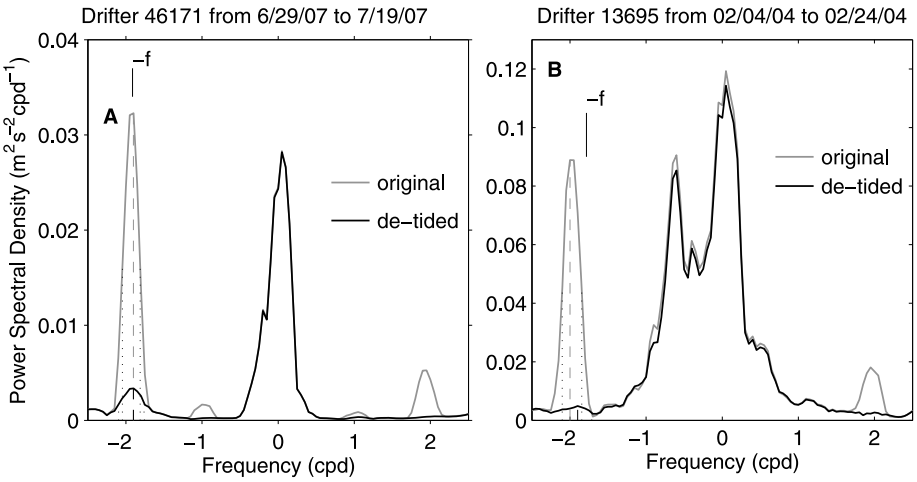

Figure 4. (a) Spectral estimates for drifter 46171 (AOML identification number) from 29 June 2007 to 19 July 2007 for the original time series (gray curve) and for the detided time series (black curve). Here $-f$ denotes the mean inertial frequency for this trajectory segment. Dotted lines on each side of the inertial peaks in both spectra indicate the half power cutoff frequencies. In this case, an inertial peak is still diagnosed after detiding the original time series. (b) Same as in Figure 4a but for drifter 13695 from 2 February 2004 to 24 February 2004. In this case no more inertial peak is diagnosed after detiding.

well be the case that genuine NIOs had their frequency close to a tidal frequency. To minimize erroneous diagnoses, we decided to discard cases for which the frequency of the near-inertial peak was within the diurnal or semidiurnal tidal bands (plus half a frequency resolution bandwidth) defined by the first eight major components, but for which the expected inertial frequency was located outside these bands. Discarding all the data with expected or diagnosed peak frequencies within tidal bands does not change qualitatively the conclusion of this study.

3.4. Rotary Coefficient

[20] We used another criteria to distinguish NIOs from other types of variability: the polarization of the rotary spectrum S at the near-inertial peak, adapted from *Gonella* [1972]

$$r(f_p) = \frac{S(-f_p) - S(f_p)}{S(f_p) + S(-f_p)}, \tag{4}$$

where f_p is the frequency of the near-inertial peak. Here, $r = -1$ for purely circular anticyclonic oscillations. The theoretical polarization of a freely propagating internal gravity wave is a function of its intrinsic frequency and the local Coriolis frequency [*Elipot and Lumpkin*, 2008] and is less than −0.9 for near-inertial waves shifted as much as ±30% at all latitudes considered here. We decided to retain only the cases for which $r(f_p)$ was less than 0 (which means that the variance is more than 50% anticyclonic). Note that we see no reason why there could not be predominant cyclonic oceanic variability at f (rather than at the inertial $-f$, R. Lumpkin and S. Elipot, Surface drifter pair spreading in the North Atlantic, submitted to *Journal of Geophysical Research*, 2008) but we decided not to include such cases to limit the noise surrounding the phenomena we are interested in.

3.5. Meridional Drift

[21] A surface drifter changes latitude with time so that it is reasonable to expect that this could shift or broaden the inertial peak [*Lilly and Olhede*, 2009] (see also section 4). We attempt to quantify the impact of the meridional drift by estimating $\beta y_{\mathrm{RMS}}/|f|$ where y_{RMS} is the root mean square meridional drift computed from the mean latitude of a 20 day segment. The distribution of this term for the data retained for this study is shown in Figure 5.

[22] Several percentile values of the distribution are superimposed on this plot which indicate that the expected relative frequency shift from drift should be less than 0.7 % for 50% of the data, less than 2.7% for 95% of the data and less than 4.7% for 99% of the data. On average, the effect of

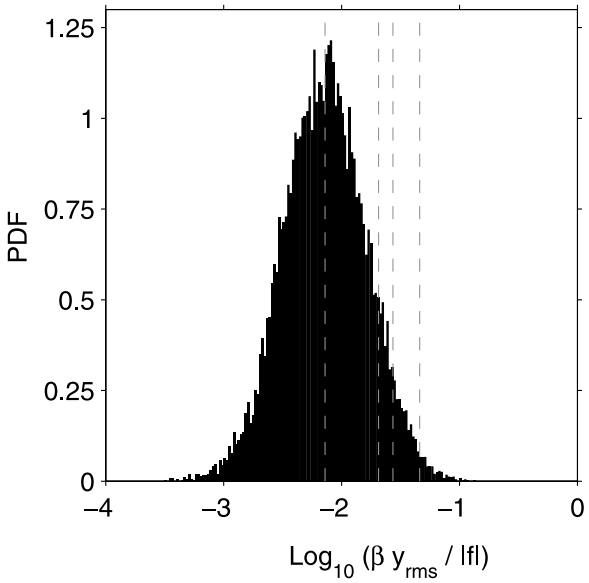

Figure 5. Distribution of $\log_{10} \beta y_{\mathrm{RMS}}/|f|$ for all the 20 day trajectory segments retained for this study. The vertical dashed lines from left to right indicate the 50, 90, 95, and 99 percentiles of the distribution.

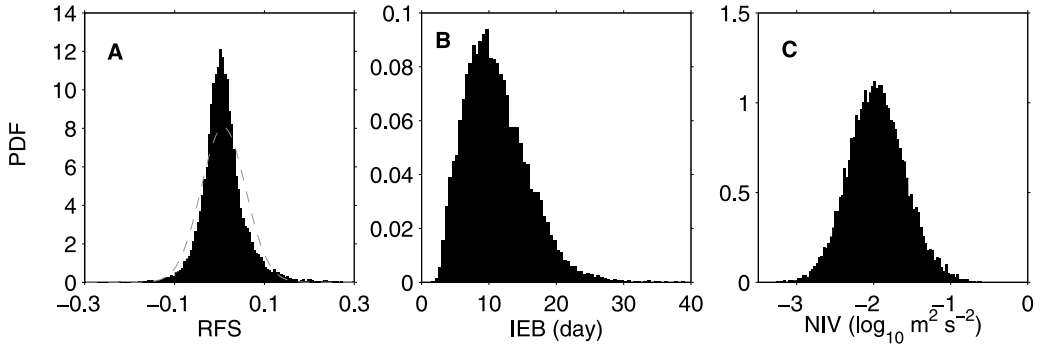

Figure 6. Probability density functions (pdf) for (a) the relative inertial frequency shift along with a Gaussian distribution with the same mean and standard deviation (dashed curve), (b) the inverse excess bandwidth, and (c) the near-inertial variance.

the meridional drift with respect to the mean position of a drifter appears to cancel out because the frequency shift is measured from the inertial frequency of the mean latitude over 20 days. Furthermore, we could not see a significant relationship between the meridional drift of the 20 day trajectory segments and the characteristics of the NIOs, particularly when examining the influence of the mesocale. Excluding data points for which the drift term is large does not change the qualitative conclusions of our global analysis.

4. Observations of Relative Frequency Shift, Inverse Excess Bandwidth, and Near-Inertial Variance

[23] In this section, we first examine how characteristics of NIOs introduced in section 3 vary globally and as a function of geographical location. Our data set consists of 19,472 concurrent estimates of RFS, IEB and NIV.

4.1. Probability Distribution Functions and Geographical Distribution

4.1.1. RFS

[24] Observed RFS are in the [−0.3, 0.3] interval with very few outliers that were discarded. The mean of the RFS global distribution (Figure 6a) is 0.0086 and the standard deviation is 0.049. A chi-square goodness of fit rejects the null hypothesis at the 5% level that this distribution is Gaussian. The distribution is skewed positive (skewness parameter 0.65) and its excess kurtosis, a measure of the peakiness of the distribution, is greater than 3. All together this suggests that it is reasonable to seek a deterministic origin for such a distribution.

[25] Later in this paper we will show that the frequency shift is associated with mesoscale geostrophic vorticity. Anticipating this result now, we may hypothesize that the nonzero mean RFS indicates preferential sampling of cyclonic over anticyclonic vortices by drifters [*Middleton and Garrett*, 1986]. However, a linear regression of RFS against the geostrophic vorticity shows that even in the absence of vorticity, the frequency shift is nonzero and positive. This suggests that a potential sampling bias toward cyclonic regions cannot alone account for the nonzero mean of the RFS distribution.

[26] Figure 7 shows two maps of the 20 day trajectory segments colored by their RFS, one for which the RFS are positive (Figure 7 (bottom)) and one for which they are negative (Figure 7 (top)). The positive and negative sides of the color scale are histogram equalized such that each discrete color step comprises 10% of the realizations of the positive or negative shifts. A linear color scale would not be ideal here because about 78% of the data have a RFS between −0.05 and 0.05.

[27] The average RFS is computed in 1° bins (Figure 8 (top)), with each hourly drifter position associated with the RFS of the whole trajectory segment it belongs to and counting for one observation when computing the average. Thus, the computation of the mean is weighted by the length of time that a drifter spend in each box. No mean was computed in boxes that were crossed by only one trajectory segment. We recognize that these estimates of the mean are not always significant (see standard deviation of RFS in Figure 8 (bottom)), and may be biased by the drifter sampling; but it still shows significant features.

[28] On a global scale, poleward of approximately 30°N or S, the mean RFS is relatively small, without a clear sign, such as in the middle of the subtropical gyres. In fact, many regions where large positive frequency shifts occur coincide with regions where large negative shifts also occur, e.g., in western boundary currents and their extension regions, and around the Antarctic Circumpolar Current (Figure 7).

[29] Equatorward of 30°, the mean RFS is predominantly positive, with values above 0.06 in some bins saturating the color scale. If the mean RFS is computed as a function of latitude (not shown), using only data for which the relative vorticity divided by f is less than 0.01 to minimize the influence of the background flow, it is significantly greater than 0.01 only approximately equatorward of 30°N or S (between 0.02 and 0.05). This positive or "blue" shift (in analogy to the spectrum of visible light) can be interpreted in the context of the generation and propagation of near-inertial waves on the globe [*Fu*, 1981]: having been generated near their inertial latitude (most likely under the atmospheric storm track at midlatitudes equatorward of 30°), near-inertial waves are free to propagate between their inertial latitude and the equator and therefore will always have a frequency higher than the local inertial frequency [e.g., *D'Asaro*, 1995; *Garrett*, 2001; *Alford*, 2003; *Elipot and Lumpkin*, 2008]. Validating this interpretation would require relating the observed NIOs to atmospheric forcing in order to determine if they were locally forced or resulting from propagation, an analysis which extends beyond the scope of this study.

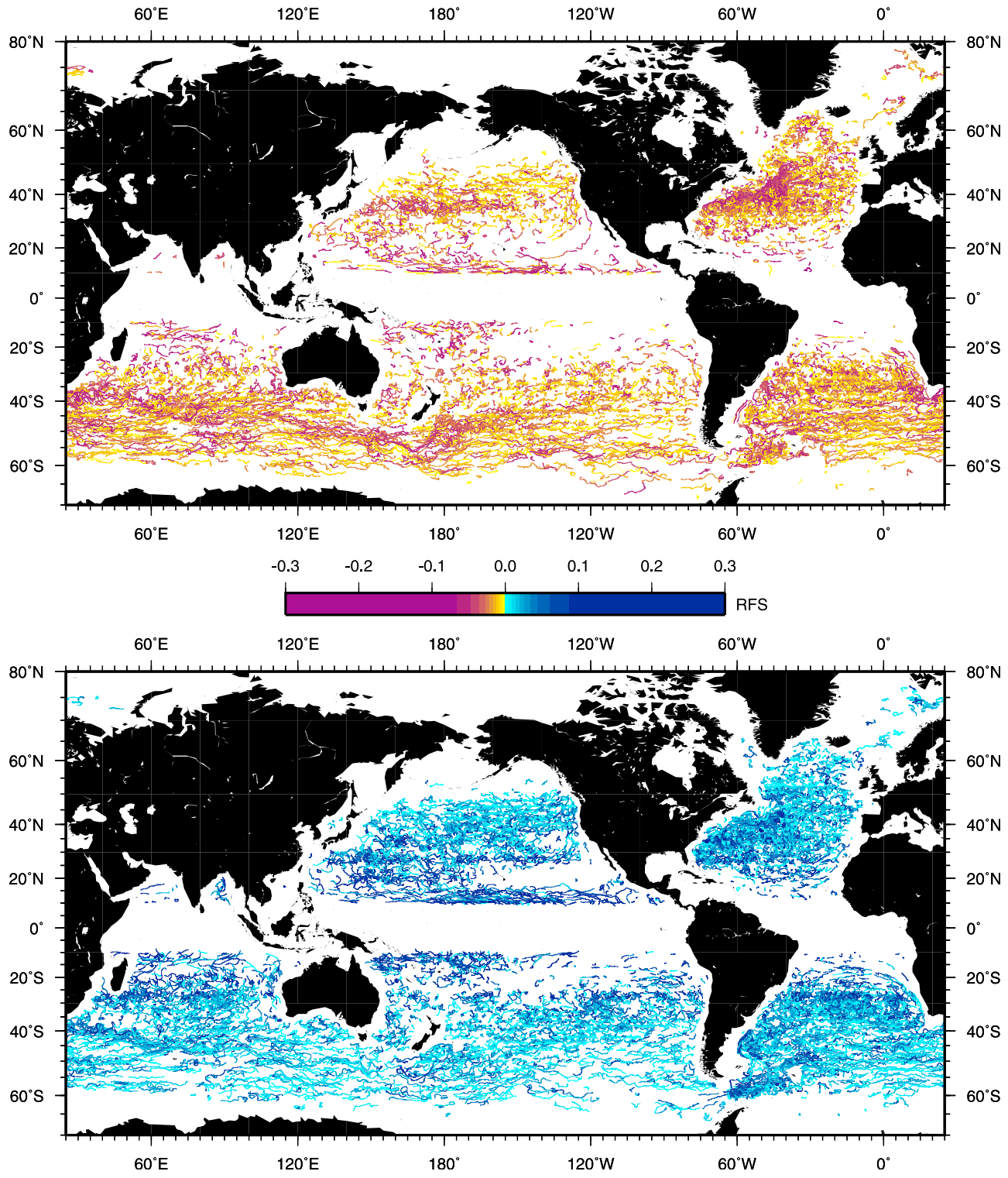

Figure 7. The 20 day trajectory segments color coded for their RFS. (top) Negative relative frequency shift and (bottom) positive relative frequency shift.

[30] At smaller spatial scales, the map of mean RFS shows a band of negative values along the anticylonic (north) side of the Agulhas Retroflection, and a band of positive values on its cyclonic side. The same pattern is noticeable along the Gulf Stream, downstream of Cape Hatteras. An area of negative RFS east of South Africa is quite noticeable. Positive mean values of RFS larger than 0.06 are also found in patches east of Drake Passage and on the Macquarie Ridge but these values may be associated with semidiurnal baroclinic tidal peaks rather than genuine inertial peaks (see section 3).

[31] The standard deviation of RFS is computed in 1° bins (Figure 8 (bottom)) in the same way as the map of mean

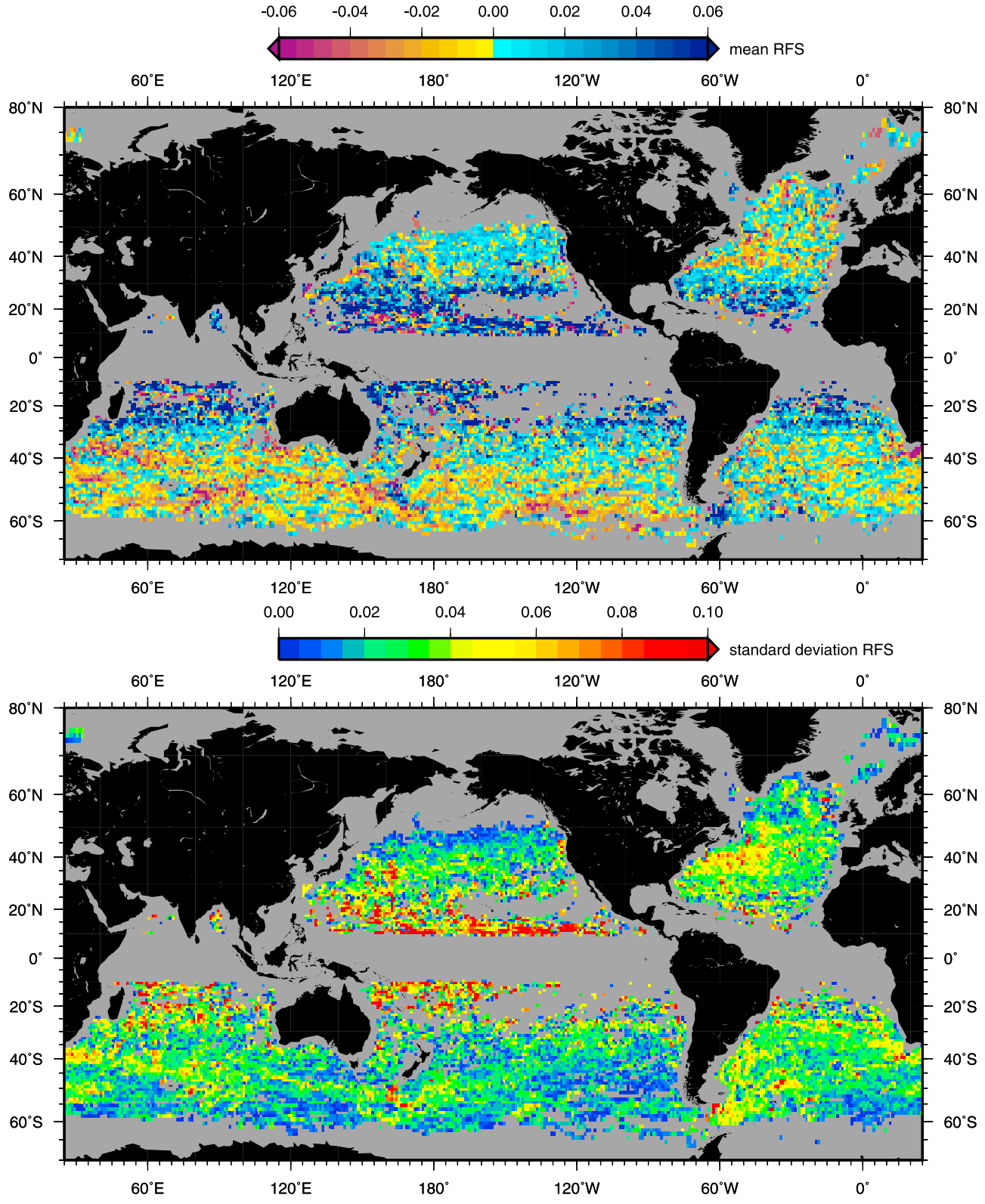

Figure 8. (top) Average and (bottom) standard deviation of RFS in 1° bins.

RFS. Regions of large standard deviations correspond approximately to large eddy kinetic energy regions previously estimated by altimetry or historical drifter data [e.g., *Stammer*, 1997; *Lumpkin and Pazos*, 2007]: in boundary currents and their extension regions as well as along the Antarctic Circumpolar Current, between 10° and 20° in the North and South Pacific and along 20°S in the Indian Ocean. The map of RFS standard deviation suggests that regional

characteristics of NIOs can vary substantially. The relationship of these variations to the geostrophic mesoscale field is further investigated in section 5.

4.1.2. NIV

[32] The global probability distribution function of the decimal logarithm of observed NIV (Figure 6c) is unimodal with a modal value of −2, implying that typical root-mean-square NIOs magnitude is 0.1 m s^{-1}. The mean NIV is computed in 1° bins (Figure 9 (bottom)), as well as the mean near-inertial energy (Figure 9 (top)) $0.5\rho H U_{\mathrm{RMS}}^2$ in J m^{-2} where U_{RMS}^2 is equal to NIV, and where it is assumed that near-inertial currents are vertically uniform over the depth H of the mixed layer [e.g., *Chaigneau et al.*, 2008]. H was estimated from a seasonal climatology derived from hydrographic and Argo float data by *de Boyer Montegut et al.* [2007], and ρ was taken at the nominal value of 1025 kg m^{-3}.

[33] In general, the largest values of NIV or energy are found at midlatitudes in all basins, under the atmospheric storm tracks. These regions include the midlatitudes of the North Pacific and South Atlantic, and to a lesser degree the North Atlantic. In terms of their distributions, these two maps differ most dramatically in the Southern Ocean. There, the mixed layer depth can reach many hundreds of meters, consequently generating large values of energy if the inertial currents are truly uniform in the vertical.

[34] Overall, these estimates are consistent with the zonally averaged inertial variance estimates from surface drifters in each ocean basin by *Elipot and Lumpkin* [2008], as well as the inertial current amplitude and energy maps of *Chaigneau et al.* [2008], and the estimates of *Park et al.* [2005] from Argo floats.

4.1.3. IEB

[35] The global probability distribution function of IEB (Figure 6b) is unimodal with a modal value of approximately 10 days, which would correspond to an exponential decay time scale of approximately 3 days (see Figure 3c).

[36] The global map of 1° mean IEB (Figure 10) is rather noisy but some spatial patterns emerge. IEB is larger at midlatitudes. In fact, this map roughly corresponds to the spatial patterns found in the map of mean NIV (indicating a relationship between NIV and IEB), except in some regions of strong geostrophic currents like the Gulf Stream, the Agulhas Retroflection and the Kuroshio Extension regions, where IEB is shorter. We will examine more closely how the relationship between IEB and NIV can break down by considering the relationship between IEB and the geostrophic mesoscale in section 5.

[37] Our estimates of decay time scale by the IEB are compatible with the results of *Park et al.* [2009] who estimated the global distribution of decay time scale in zonal bands in each ocean basin. Their estimates are based on e-folding time scales of temporal correlation functions of surface drifter velocity time series. Consistent with that study, we also observe that the decay time scale does not increase with latitude in the North Atlantic as it does in the North Pacific. *Park et al.* [2009] shows that this is the result of the buoyancy structure of the North Atlantic, which compensates for the the effect of β on near-inertial wave phase dispersion.

4.2. Characteristics: Intrinsic Relationships

[38] We examine now how the three characteristics considered (RFS, IEB, and NIV) vary with respect to each other. For this, we consider the means and distributions of each characteristic when sorted in bins of each of the other two. In order to minimize the impact of outliers in the data distributions, we selected the edges for binning as the first and 99th percentiles of each of the distributions shown in Figure 6. The bins are of uneven width such that their boundary values correspond to the first percentile, third, 5th, and so on through the 99th percentile.

[39] NIV is maximum when NIOs are the least shifted in frequency, that is when RFS is near zero (Figure 11a). Inversely, RFS generally decreases with increasing NIV (Figure 11f) but this tendency is not as clear when only data poleward of 30° are used (not shown).

[40] NIV increases almost linearly with IEB up to approximately 20 days (Figure 11b) but the distribution in each bin is wide. This linear relationship also holds when IEB is computed as a function of NIV (Figure 11d). This is expected from a sampling point of view: when near-inertial oscillations last longer, surface drifters capture more variance over their 20 day trajectories (see section 3 and Figure 3). An apparent consequence is that IEB is maximal when the RFS is near zero (Figure 11c). However, RFS itself is mostly independent of IEB and lies just below 0.01 (Figure 11e) but is slightly higher when IEB is less than 5 days. If only data poleward of 30° are used, RFS is marginally positive for almost all IEB less than 17 days.

[41] In summary, NIOs are observed to have longer time scales (or are more persistent, according to *Fu*'s [1981] interpretation) when they are of larger variance, but this may be due to the sampling. More interestingly, the largest NIOs with the longer time scales are the least shifted in frequency. Why this relationship is observed in a globally average sense is not clear.

5. Modification by the Mesoscale Geostrophic Flow

[42] We now turn our attention to NIO characteristics as a function of the characteristics of the vorticity field. We first review theoretical expectations, then describe the altimetry-derived vorticity field. We then present our observations of the modification of NIO characteristics by the vorticity.

5.1. Theoretical Predictions

5.1.1. *Kunze*'s [1985] Paradigm

[43] The dispersion relation for a near-inertial wave in the presence of a mean quasigeostrophic flow $\mathbf{V} = (U, V, W)$ is derived by *Kunze* [1985]. The derivation involves all nonlinear terms because it is assumed that the quasi-geostrophic flow and the near-inertial wave flow can have similar scales. If it is assumed that locally the solution ψ is in the form of a plane wave, i.e.,

$$\psi = \psi_0 \exp[i(\mathbf{k}\cdot\mathbf{x} - \omega t)], \quad \mathbf{k} = (k_x, k_y, k_z), \quad \mathbf{x} = (x, y, z), \quad (5)$$

the dispersion relation is complex and its real part states that the Lagrangian intrinsic frequency of the wave, i.e., the Eulerian frequency of the wave ω minus the Doppler shift from the mean flow, is approximately

$$\sigma = \omega - \mathbf{k}\cdot\mathbf{V} \approx \left[f_{\mathrm{eff}} + \frac{N^2 k_H^2}{2fk_z^2} + \frac{1}{k_z}\left(\frac{\partial U}{\partial z}k_y - \frac{\partial V}{\partial z}k_x\right)\right], \quad (6)$$

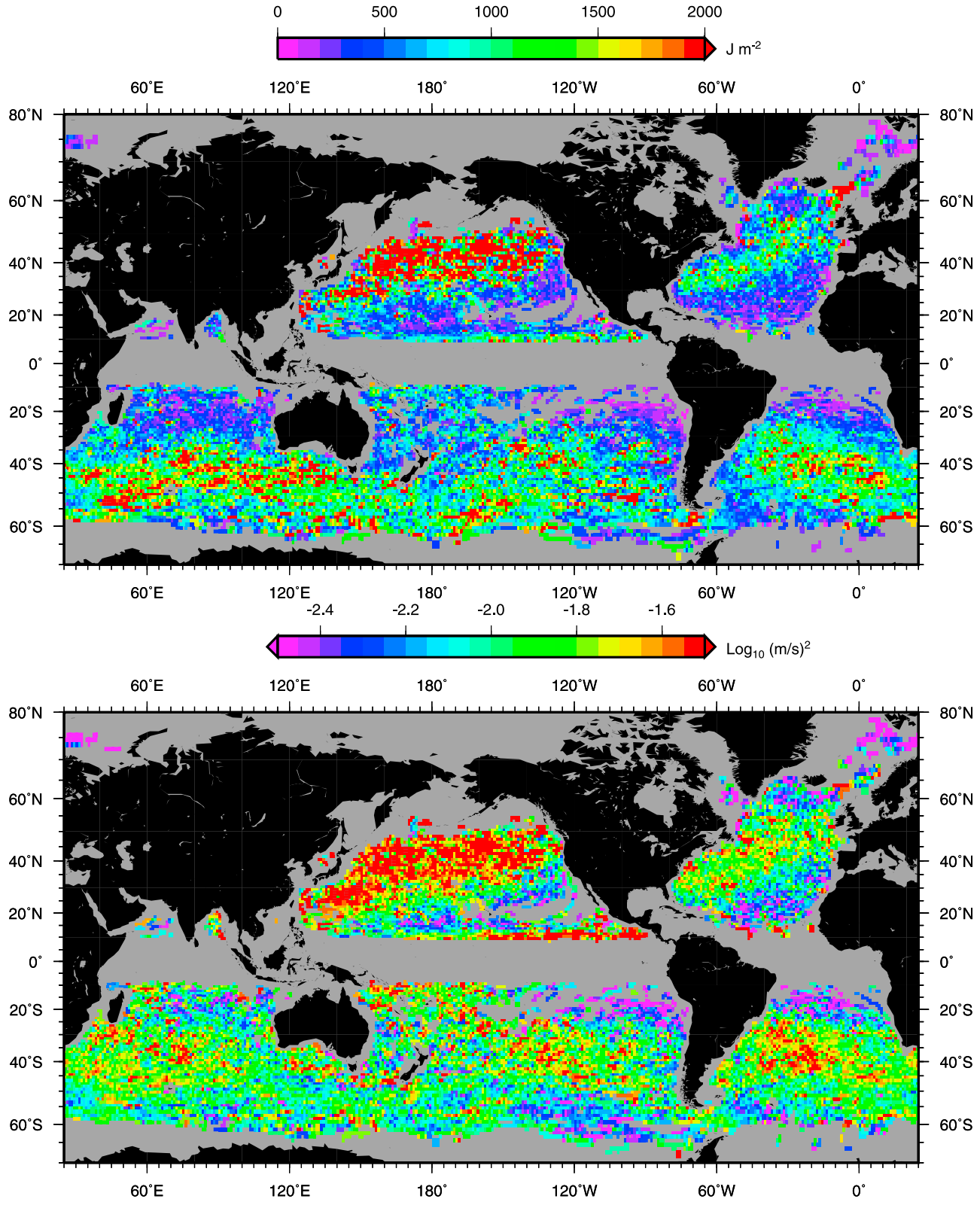

Figure 9. (bottom) Average NIV and (top) near-inertial energy in 1° bins.

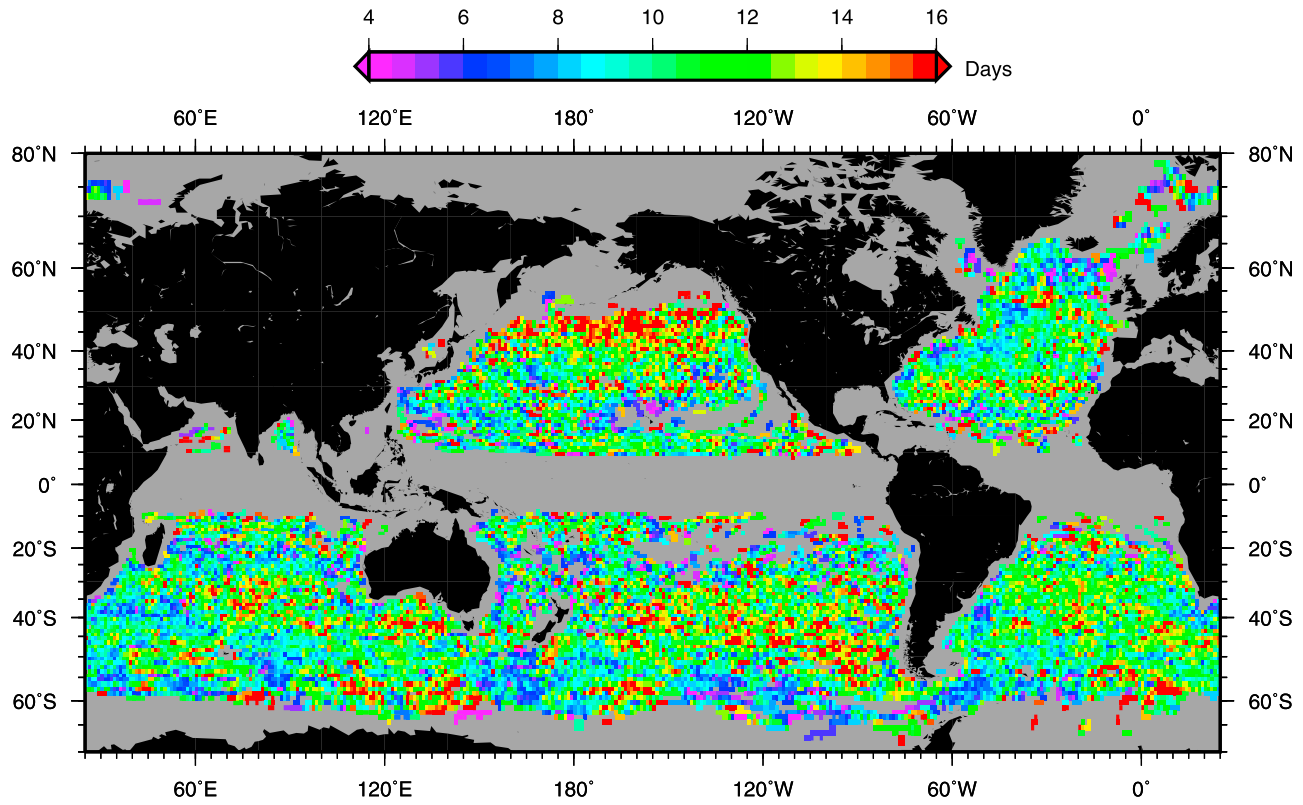

Figure 10. Average IEB in 1° bins. The color scale saturates for values less than 4 days and more than 16 days.

where $k_H = \sqrt{k_x^2 + k_y^2}$ is the horizontal wave number, N the buoyancy frequency and f_{eff} the effective inertial frequency defined by

$$f_{\text{eff}} = \left[f^2 + f\left(\frac{\partial V}{\partial x} - \frac{\partial U}{\partial y}\right) - \frac{\partial V}{\partial x}\frac{\partial U}{\partial y} + \frac{\partial U}{\partial x}\frac{\partial V}{\partial y} \right]^{1/2}. \quad (7)$$

For small Rossby number flow,

$$f_{\text{eff}} \approx f + \frac{\zeta}{2} = F + \frac{1}{2}\left(\frac{\partial V}{\partial x} - \frac{\partial U}{\partial y}\right). \quad (8)$$

In a region of vorticity ζ, the local rotation rate is $\zeta/2$ and consequently a wave experiences an advective rotation $\zeta/2$ in addition to the planetary vorticity f. *Poulain et al.* [1992] derived inertial wave characteristics from surface drifters in the Tropical Pacific and showed qualitative agreement between the observed frequency of NIOs and the predicted frequency shift by the local vorticity as described by equation (8). The dispersion relation (6) gives the range of frequency over which internal gravity wave can exist. For the lower bound of the spectrum, when $k_H/k_z \to 0$ in the case of a barotropic mean flow, the lowest frequency of a near-inertial wave is not f as it would be in the absence of mean flow shear but rather f_{eff}. *Kunze* [1985] notes that in region of negative vorticity, f_{eff} is lower than f so that the internal wave spectrum is enlarged and potentially more energy can be input by the wind at the ocean near surface.

[44] *Kunze* [1985] studied the propagation of near-inertial waves generated at the surface for idealized cases of barotropic and baroclinic jets. A ray tracing analysis suggests that trapping of near-inertial waves should roughly occur in regions of anticyclonic vorticity, if the waves are generated in the anticyclonic regions themselves. The lower effective inertial frequency of the waves prevent them from propagating outside the anticyclonic regions. This phenomenon is often invoked to interpret observations of increased levels of near-inertial activity. As an example, *Shcherbina et al.* [2003] saw intensification of energy flux consistent with the trapping of near-inertial wave in an anticyclonic region but also found trapping in a cyclonic region in the subpolar front of the Japan/East Sea. *Rainville and Pinkel* [2004] suggested that the large cross-front vorticity gradient in the Kuroshio may condition the observed field of high-wave-number waves in this region.

5.1.2. *Young and Ben Jelloul*'s [1997] Approach

[45] *Young and Ben Jelloul* [1997] considered the evolution of NIOs in a three-dimensional geostrophic turbulent mesoscale field. Starting from their approach, *Danioux et al.* [2008] studied numerically the propagation of the wind energy into the deep ocean. Their results matched some analytical results of *Young and Ben Jelloul* [1997], notably how the NIO energy is organized by the Laplacian of the vorticity rather than the vorticity itself.

[46] With the condition of vertical scale separation between the geostrophic flow and NIOs, the formalism of *Young and Ben Jelloul* [1997] with the notation of *Danioux et al.* [2008] is

$$\mathcal{A}_n = \mathcal{R}_n e^{i\theta}, \quad (9)$$

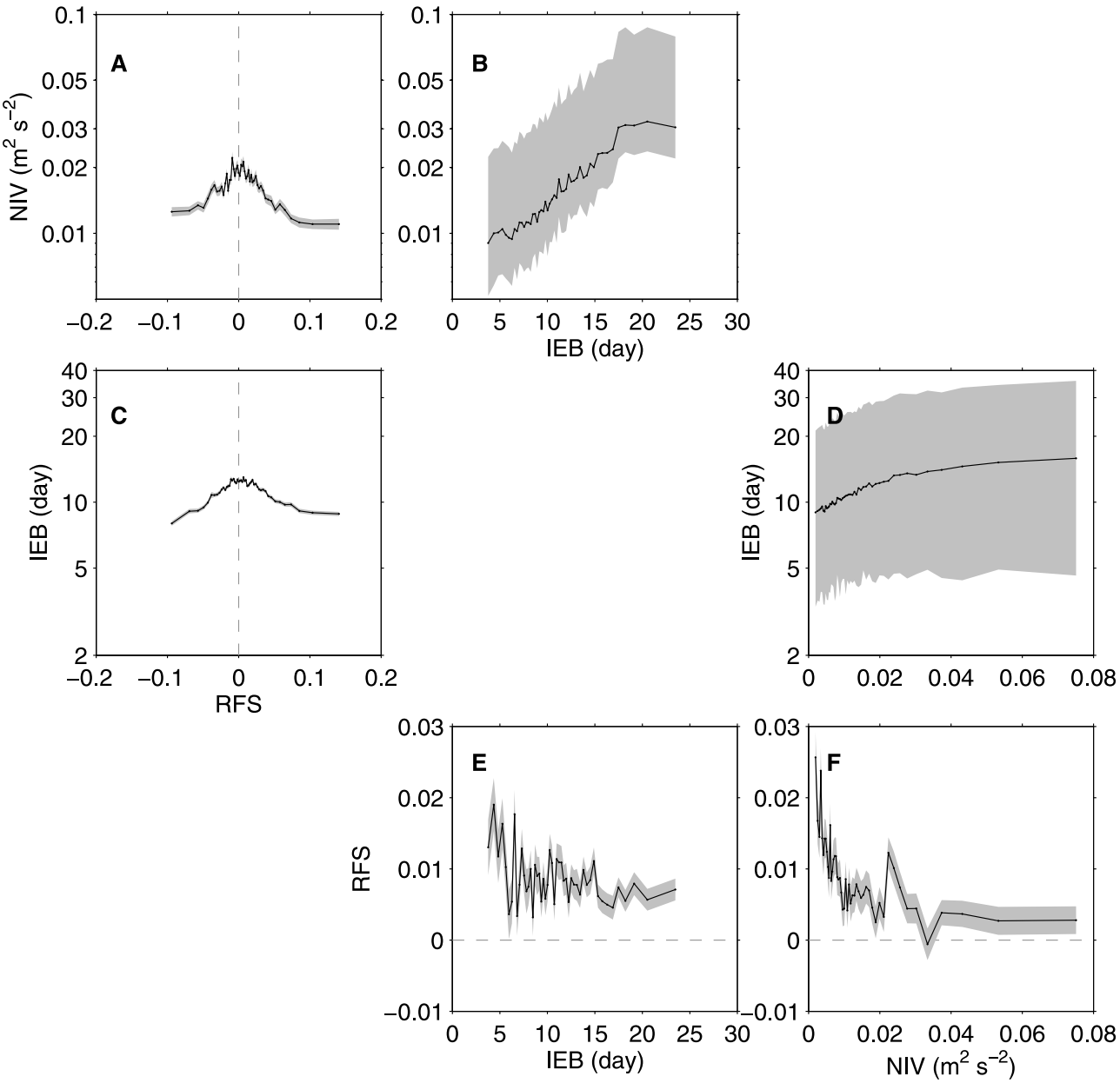

Figure 11. The mean values of each three NIOs characteristics (RFS, IEB, and NIV) as a function of one another. The gray shading corresponds to the standard error of the mean for each bin except in Figures 11b and 11d, where they correspond to the 16th and 84th percentile of the distribution in each bin.

which describes the subinertial time evolution of the amplitude $\mathcal{R}_n$ and phase θ_n of the nth eigen mode $\mathcal{A}_n e^{-ift}$ of the vertical expansion of the near-inertial velocity [e.g., *Flierl*, 1978]. This leads to a linearized system of two coupled equations for $\mathcal{R}'_n$ and θ'_n, the small departures from the initial uniform value $\mathcal{R}_{0n}$ and θ_{0n}

$$\frac{\partial \theta'_n}{\partial t} = -\frac{\zeta}{2} + \frac{r_n^2 f}{2}\frac{\nabla^2 \mathcal{R}'_n}{\mathcal{R}_{0n}}, \tag{10}$$

$$\frac{\partial \mathcal{R}'_n}{\partial t} = -\mathcal{R}_{0n}\frac{r_n^2 f}{2}\nabla^2 \theta'_n, \tag{11}$$

where r_n is the Rossby radius of deformation of mode n. The first equation represents the dispersion of the phase (refraction) and the second equation represent the dispersion of the amplitude. After generation of a uniform NIO by the wind, a solution at earlier times for the phase is $\theta'_n \approx -\zeta t/2$ [*Danioux et al.*, 2008], which is equivalent to the $\zeta/2$ frequency shift of *Kunze* [1985]. For the NIO amplitude, $\mathcal{R}'_n \approx r_n^2 f t^2 \nabla^2 \zeta/8$, i.e., the amplitude field resembles the Laplacian of vorticity $\nabla^2\zeta$. *Klein et al.* [2004a] found this solution to be one of the two exact and possible solutions for NIOs with spatial scales larger than a critical length scale $\sqrt{2\pi r_n^2 tf}$, but under the condition that the horizontal wave number spectrum of vorticity has a slope gentler than −4.

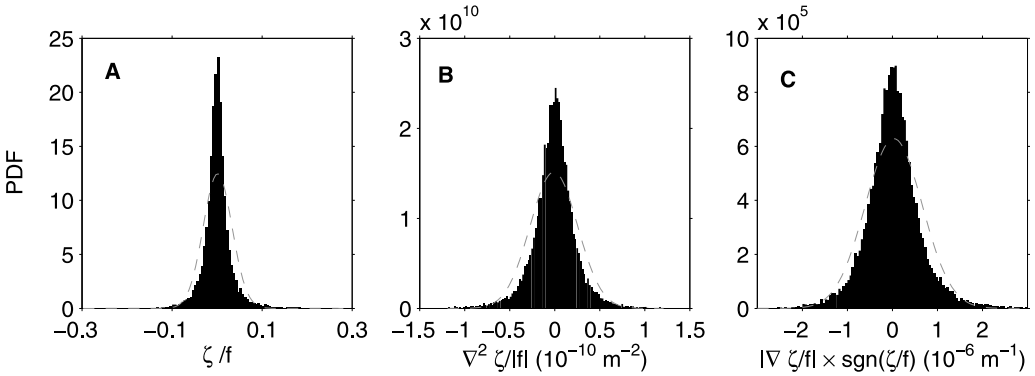

Figure 12. Probability density functions for (a) relative vorticity anomaly ζ/f, (b) Laplacian of the relative vorticity divided by the absolute inertial frequency $\nabla^2\zeta/|f|$, and (c) magnitude of the vorticity gradient divided by the absolute inertial frequency $|\nabla\zeta/f|$ and multiplied by the sign of ζ/f. The gray curve is a Gaussian distribution with the same mean and standard deviation than each distribution.

[47] *van Meurs* [1998] conjointly studied the Ocean Storms Experiment surface drifter data set and the results from a theoretical analysis and numerical experiments. He stressed the importance of the gradient of vorticity $\nabla\zeta$, which acts like β by increasing the separation of the NIO vertical modes. As a consequence, the variability of NIOs is affected by vorticity as their time decay is sped up in regions of high-vorticity gradient.

5.2. Observations of the Vorticity and Its Derivatives

[48] The previous considerations prompt us to analyze NIO characteristics as a function of the relative vorticity ζ/f, its Laplacian $\nabla^2\zeta/|f|$ and its gradient $|\nabla\zeta/f|$ times the sign of the vorticity to distinguish gradients in cyclonic or anticyclonic regions. We also consider the eddy kinetic energy of the geostrophic flow $EKE = (U^2 + V^2)/2$. The vorticity is estimated such that $\zeta/f > 0$ corresponds to a region of cyclonic relative vorticity in both hemispheres. These quantities are estimated along drifter trajectories, and not homogeneously across the global ocean; the resulting values are thus representative of the vorticity field felt by the surface drifters, at the spatial resolution allowed by altimetry.

[49] The mean of the distribution of ζ/f (Figure 12a) is 0.0012 and the standard deviation is 0.03. This implies that the Rossby number of the geostrophic flow is small, a result certainly influenced by the low resolution of the altimetry data. The distribution of ζ/f fails a chi-square goodness of fit for Gaussianity at the 95% confidence level. The skewness parameter is 0.84, which can be interpreted as an evidence of a preferential sampling of regions of cyclonic vorticity by drifters, a behavior predicted by *Middleton and Garrett* [1986]. However, this also could be due to geographical heterogeneities of the vorticity field associated with ocean dynamics [*Hughes et al.*, 2009].

[50] The distribution of $\nabla^2\zeta/|f|$ (Figure 12b) is also non-Gaussian and is skewed negative (skewness parameter is −0.71). In the AVISO altimetry maps, which are smooth by optimal interpolation, $\nabla^2\zeta$ is generally negative in cyclonic regions and positive in anticyclonic regions (with the northern hemisphere convention that positive vorticity is cyclonic). This anticorrelation can be generally expected by considering simple geometries for the vorticity field [e.g., *Young and Ben Jelloul*, 1997; *Klein et al.*, 2004a]. Figure 13 is a typical example that shows both the relative vorticity ζ on a color scale and its Laplacian $\nabla^2\zeta$ as contours, computed from AVISO map of sea level anomaly centered on the date 23 May 2007 and the Rio05 mean dynamic topography in the region of the Gulf Stream. There is an almost exact anti-correlation between ζ and $\nabla^2\zeta$. This is seen in the estimates found in this study in a scatter plot of ζ/f versus $\nabla^2\zeta/|f|$ (Figure 14c).

[51] The mean of $|\nabla\zeta/f| \times \mathrm{sgn}(\zeta/f)$ is indistinguishable from zero and its distribution is skewed positive (Figure 12c). For the distribution of the absolute value of the vorticity gradient (not shown), about 90% of the data lays below 1×10^{-6} m^{-1}. This is of the same order as β/f, which decreases from approximately 1×10^{-6} m^{-1} at 10° to 0.1×10^{-6} m^{-1} at 60°. It is very likely that the real vorticity gradients in the ocean are larger [*Klein et al.*, 2008], and these low values are due to the low resolution of the altimetry data set: indeed, the larger gradients of relative vorticity are found mostly in the large-scale vorticity patterns, i.e., the large mesoscale eddies (Figures 14b and 13).

[52] Finally, large *EKE* values are found on average in regions of large cyclonic or anticyclonic vorticity (Figure 14a), which are therefore also regions of large magnitude for $\nabla^2\zeta/|f|$. There is considerable scatter in geostrophic *EKE* as a function of ζ/f, requiring average values to be estimated in bins in order to reveal this relationship between *EKE* and ζ/f.

5.3. Observations of NIOs Modifications by the Mesoscale

[53] The characteristics of NIOs are now binned with the characteristics of the geostrophic field. For each bin, the mean values and the standard errors of the mean are estimated, leaving out bins for which less than 10 observations are available.

5.3.1. Vorticity

[54] Our observations confirm the linear dependence of the RFS on the vorticity anomaly, consistent with *Kunze*'s [1985] paradigm and the solutions of *Danioux et al.*

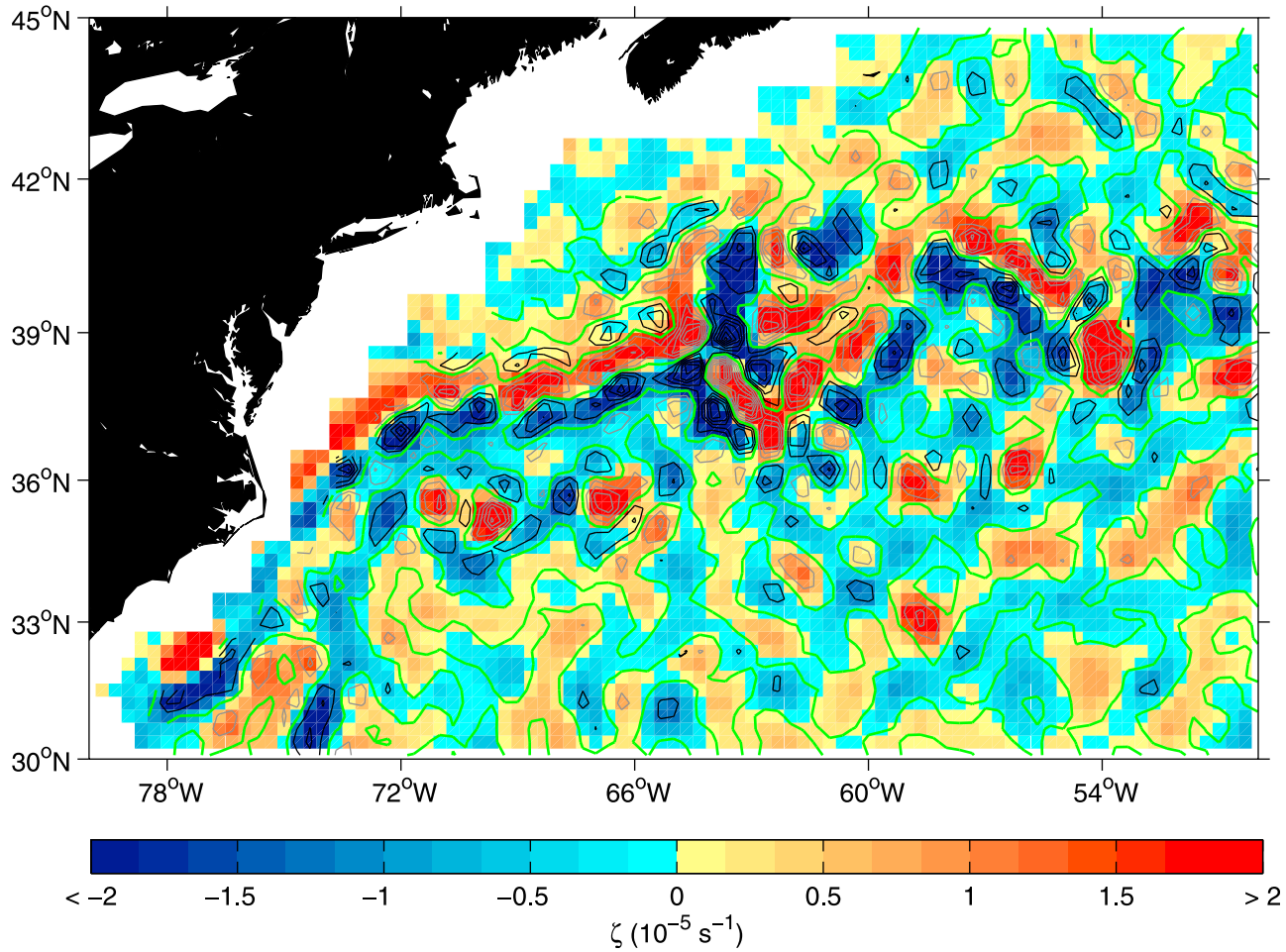

Figure 13. Vorticity ζ (shading) and Laplacian of vorticity $\nabla^2\zeta$ (contour) computed from AVISO map of sea level anomaly on 23 May 2007 and Rio05 mean dynamic topography. The zero contour for $\nabla^2\zeta$ is drawn in green, and positive contours at interval $10^{-14}\ s^{-1}\ m^{-2}$ are drawn in black and negative contours at the same interval are drawn in gray.

[2008] (Figure 15c). A weighted least-square fit gives $\Delta f/f = 0.39\zeta/f + 0.007$.

[55] The intercept of the fit suggests a globally average 0.7% blue shift (cyclonic) of NIOs at the surface. This intercept goes to zero when the data approximately equatorward of 30°N or S are discarded from the fit. This is consistent with what was previously described for Figure 8.

[56] IEB is approximately 11.5 days at zero ζ/f and decreases almost monotonically with increasing positive ζ/f (Figure 15b). IEB decreases also for increasing negative ζ/f, albeit not as strongly. This implies that the more they are shifted in frequency, the faster NIOs decay at the surface, with overall faster decay in cyclonic regions compared to anticyclonic regions.

[57] Despite the fact that on average IEB and NIV are approximately linearly related (Figure 11), the dependency of NIV on ζ/f differs from IEB (Figure 15a). Despite large error bars, NIV is overall greater in regions of anticyclonic vorticity than in regions of cyclonic vorticity. In a globally averaged sense, larger NIV is measured by surface drifters in anticyclonic geostrophic regions, consistent with trapping and possibly amplification of NIOs in anticyclonic regions.

5.3.2. Laplacian of Vorticity

[58] The RFS shows a clear linear relationship with $\nabla^2\zeta/|f|$ (Figure 16c) as expected from the anticorrelation between ζ and $\nabla^2\zeta$ (Figure 14c). Similarly, IEB is maximum near zero values of $\nabla^2\zeta/|f|$ and decreases for increasing absolute values of $\nabla^2\zeta/|f|$ (Figure 16b). However, the decrease is less pronounced for increasing positive values of $\nabla^2\zeta/|f|$, so that larger values of IEB are found in regions of positive $\nabla^2\zeta/|f|$ compared to regions of negative $\nabla^2\zeta/|f|$ of the same magnitude.

[59] NIV decreases with increasing negative values of $\nabla^2\zeta/|f|$, (Figure 16a) but a decrease for increasing positive values is not as clear. Overall, larger values of NIV are found in regions of positive $\nabla^2\zeta/|f|$ compared to regions of negative values, once again compatible with the anticorrelation of $\nabla^2\zeta/|f|$ and ζ/f and the behavior of NIV with respect to ζ/f, observed previously.

5.3.3. Gradient of Vorticity

[60] RFS is linearly dependent on the magnitude of the vorticity gradient (Figure 17c), understandable since the vorticity gradient is linearly related to the magnitude of

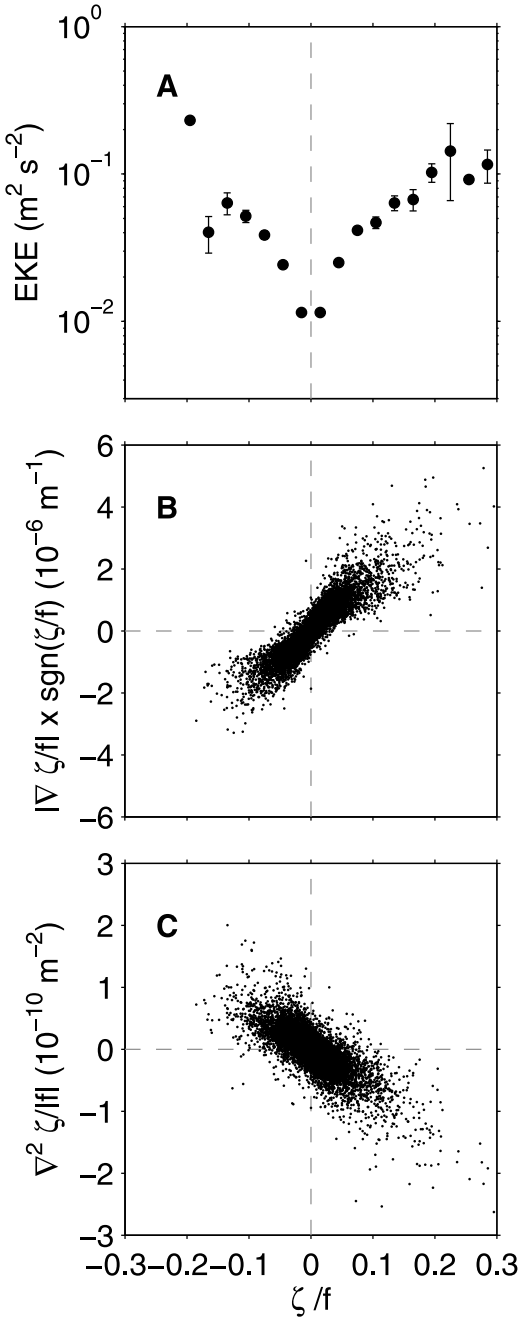

Figure 14. (a) Mean geostrophic *EKE* with standard error of the mean as a function of ζ/f. (b) Scatterplot of the magnitude of the vorticity gradient $|\nabla\zeta/f|$ times the sign of ζ/f as a function of ζ/f. (c) Scatterplot of $\nabla^2\zeta/|f|$ as a function of ζ/f.

the vorticity (Figure 14b). Near zero values of $|\nabla\zeta/f| \times \mathrm{sgn}(\zeta/f)$, RFS is positive, but this blue shift once again disappears when data within 30° of the equator are excluded from the analysis.

[61] IEB is maximum near zero values of $|\nabla\zeta/f| \times \mathrm{sgn}(\zeta/f)$ (Figure 17b), and decreases when the vorticity gradient increases, albeit not as strongly for anticylonic vorticity as for anticyclonic vorticity. In contrast, NIV does not depend on the gradient of the vorticity (Figure 17a).

5.3.4. Geostrophic Eddy Kinetic Energy

[62] The RFS is not strongly dependent on *EKE* (Figure 18c), especially considering the logarithm scale. For about 2 orders of magnitude RFS is constant at around 0.01, reflecting the global average. However, in the largest *EKE*

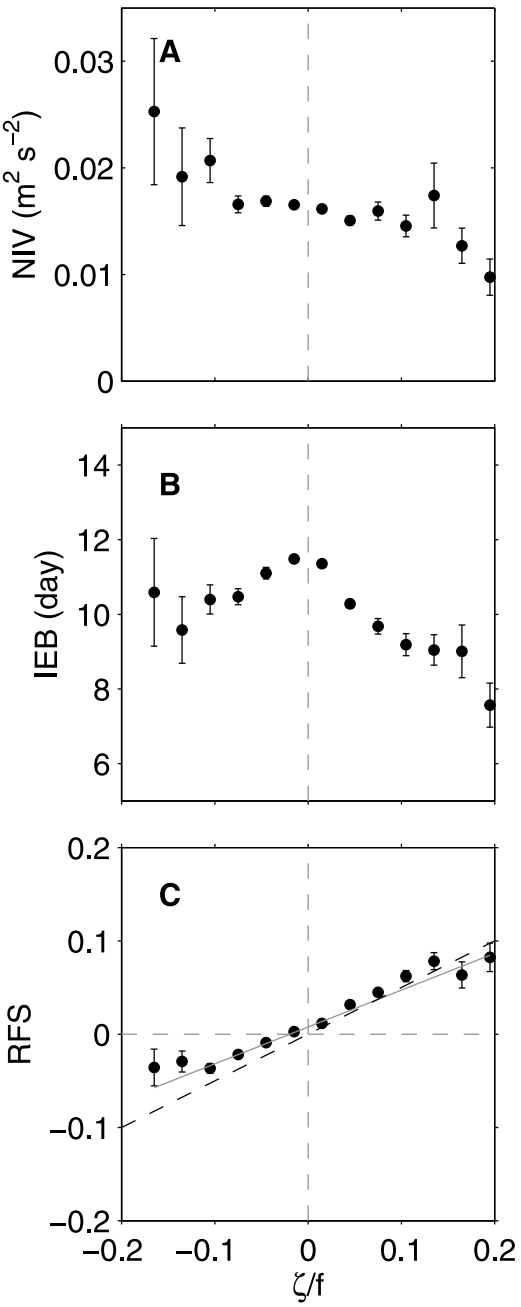

Figure 15. (a) Mean near-inertial variance, (b) mean inverse excess bandwidth, and (c) mean relative frequency shift when the data are binned by values of ζ/f. The solid gray line in Figure 15c corresponds to the weighted least-square regression on the data $\Delta f/f = 0.39\zeta/f + 0.007$. The dashed black line corresponds to the theoretical $\Delta f/f = 0.5\zeta/f$. Positive ζ/f correspond to cyclonic vorticity anomalies. Error bars correspond to the standard error of the mean in each bin.

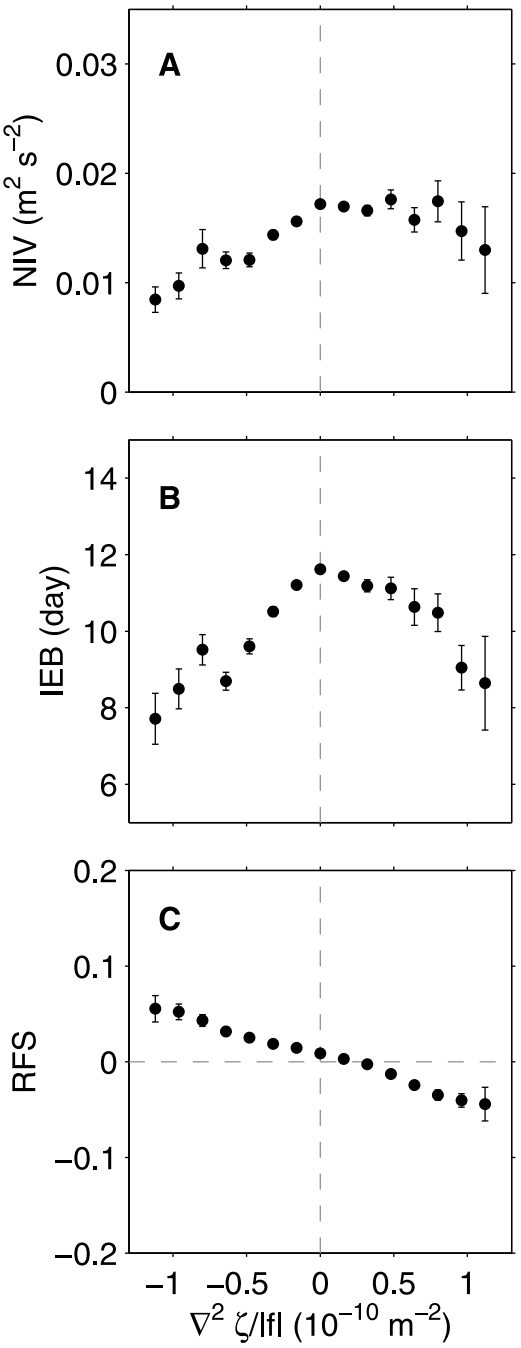

Figure 16. (a) Mean near-inertial variance, (b) mean inverse excess bandwidth, and (c) mean relative frequency shift when the data are binned by values of the Laplacian of vorticity $\nabla^2\zeta/|f|$. Error bars are standard error of the mean in each bin.

bins, RFS appears to be preferentially negative. The last bin includes only 19 data points and is unlikely to represent a significant global value. Similarly, NIV is not a function of geostrophic *EKE* on average (Figure 18a).

[63] IEB strongly depends on $\log_{10}$ *EKE* (Figure 18b): it decreases approximately linearly from about 14 days to 8 days. This is compatible with the relationships described above: large *EKE* regions are associated with large ζ/f or $\nabla^2\zeta/f$ regions in the altimeter data set (Figure 14), within which IEB is shorter.

[64] We can now understand better the geographical patterns for IEB (Figure 10). Whereas the intrinsic relationship between IEB and NIV suggests that IEB should be large where NIV is large at midlatitudes (Figure 9), this is not the case for the Kuroshio extension region, the core of the Gulf

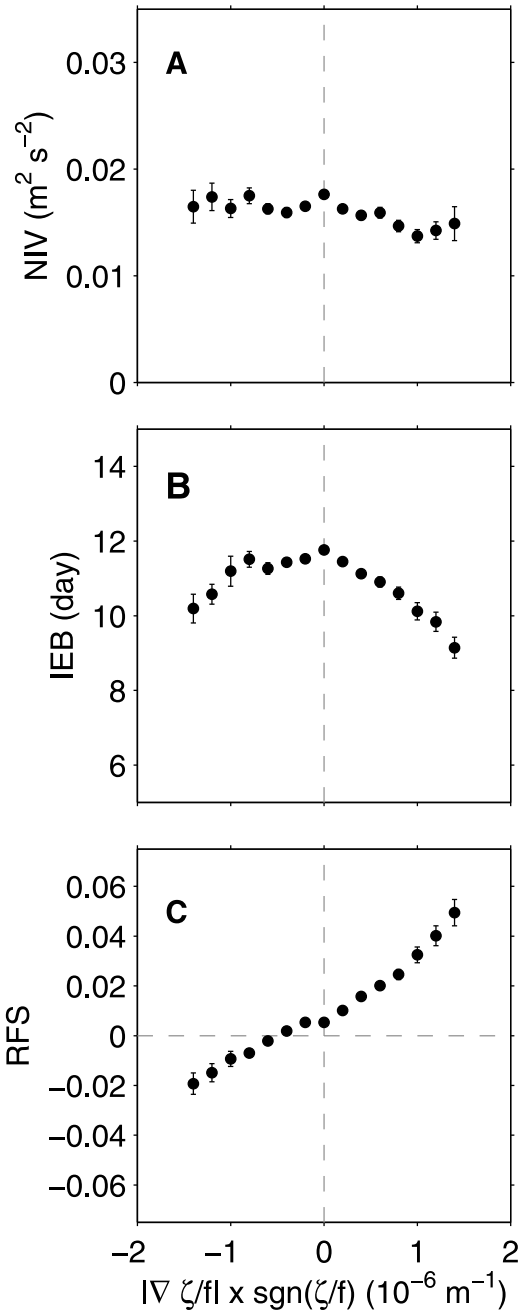

Figure 17. (a) Mean near-inertial variance, (b) mean inverse excess bandwidth, and (c) mean relative frequency shift when the data are sorted in bins of magnitude of the gradient of vorticity divided by f times the sign of the relative vorticity.

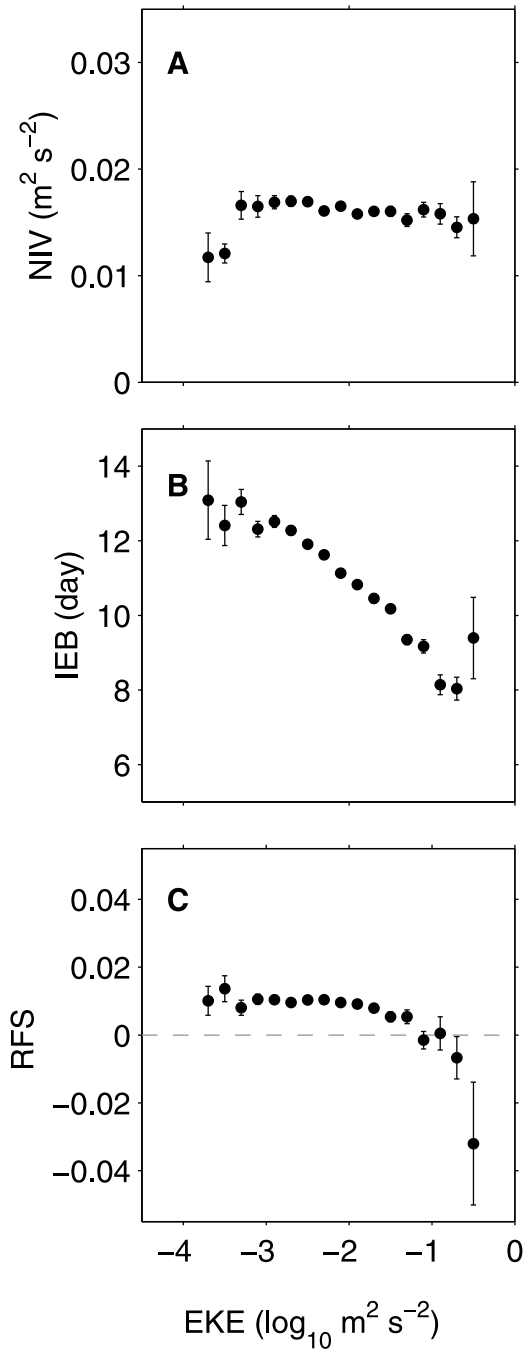

Figure 18. (a) Mean near-inertial variance, (b) mean inverse excess bandwidth, and (c) mean relative frequency shift when the data are binned by the geostrophic eddy kinetic energy $EKE = (U^2 + V^2)/2$.

Stream and along the Antarctic Circumpolar Current where the geostrophic *EKE* is larger, and IEB is therefore smaller.

6. Summary and Discussion

[65] Combining the analyses of surface drifter and altimetry data confirms that the frequency of NIOs is shifted by the geostrophic relative vorticity, in a globally average sense. The effect of the vorticity is superimposed on a global pattern; equatorward of 30°N or S, NIOs are shifted positive (a blue shift) on average by 2.5%. This blue shift may be the result of a global field of NIOs whose propagation is constrained toward the equator because of the β effect [*Fu*, 1981; *Elipot and Lumpkin*, 2008]. Because it is observed that, in the altimetry data set, $\nabla^2\zeta/f$ is anticorrelated and $|\nabla\zeta/f| \times \mathrm{sgn}(\zeta/f)$ is correlated with ζ/f, it is also observed that the frequency shift depends linearly on these quantities.

[66] If only positive ζ/f data are considered, the frequency shift agrees, within the error bars, with the theoretical 1/2 slope from *Kunze*'s [1985] paradigm. In contrast, if only negative ζ/f data are used, the frequency shift is less than 1/2 in magnitude. This is unexpected because it is commonly thought that because of the centrifugal force in a vortex-shaped eddy, the geostrophic velocity deduced from the pressure (sea level) gradient is overestimated in cyclones and underestimated in anticyclones [*Maximenko and Niiler*, 2006]. The same biases should take place for the vorticity so that if the 1/2 slope is expected for true vorticity, the slope should be smaller in cyclonic vorticity regions and larger in anticyclones; the opposite of what is found here. For $|\zeta/f| > 0.1$, the 1/2 slope is no longer observed, and the frequency appears lower than what is expected. Various reasons may be responsible. Since ζ/f is an estimate of the Rossby number of the flow, at larger values the assumption of weak geostrophic shear may not be valid anymore. Also, we assumed that the Doppler shift could be neglected as if the surface drifters were completely advected by the geostrophic flow. This assumption may not be valid when the magnitude of the geostrophic velocity becomes large and the flow feature rapidly passes a drifter, introducing a Doppler shift to the frequency felt by a drifter.

[67] Finally, NIOs at the surface eventually develop finite horizontal scales so that the dispersion relation (equation (6)) from *Kunze*'s [1985] theory can no longer be taken in the approximation $k_H/k_z \rightarrow 0$. Similarly, in the solutions of *Danioux et al.* [2008], the $\zeta/2$ phase shift is predicted at the earliest times of the solution only, that is just after generation of a spatially uniform NIO by the wind. At later times, it is predicted that inhomogeneities in the NIO field itself, i.e., the development of finite length scales, should play a role in the dispersion of the phase (see equation (10)).

[68] Our observed geographical patterns of NIV are consistent with other global analyses [*Park et al.*, 2005; *Chaigneau et al.*, 2008; *Elipot and Lumpkin*, 2008]. *Chaigneau et al.* [2008] showed that the *Pollard and Millard* [1970] slab layer model forced by scatterometer winds is unable to reproduce their global observations. In fact, *Plueddemann and Farrar* [2006] showed that it is necessary to take into account the interactions with the stratification below the mixed layer to better model the near-inertial energy. Our results suggest that the geostrophic mesoscale also plays a role in shaping the geography of NIOs, not only in term of RFS but also for NIV.

[69] We are able to partially confirm some theoretical and numerical predictions about the organization of near-inertial energy by a rich field of mesoscale eddies. The observed NIV at the surface depends upon the geostrophic vorticity: it is approximately maximum for near zero values of the Laplacian of the vorticity, and decreases for nonzero values, albeit not as much for positive as for negative values. As a consequence, more NIV is found in anticyclonic vorticity

regions than in cyclonic vorticity regions. Figure 16 is not unlike Figure 13a of *Danioux et al.* [2008] which shows how the near-inertial horizontal energy of the third vertical mode of NIOs varies as a function of the Laplacian of vorticity in a numerical simulation. They found that this result is also applicable to the other modes.

[70] Our values of NIO decay time scales, via the analysis of the excess bandwidth of the velocity spectrum, are intrinsically linked to our observation methods: more near-inertial variance over the analyzed time series is associated with longer diagnosed time scale. Like NIV, IEB is generally shorter when the vorticity or the Laplacian of vorticity is larger. Yet while NIV is largely independent of the gradient of the vorticity, IEB decreases with increasing gradient, an observation consistent with the results of *van Meurs* [1998] who showed the same phenomenum from drifter observations and numerical simulations. If one interprets the time scale of the evolution of surface NIOs as being the time necessary for the near-inertial energy to propagate vertically downward, our observations are consistent with the concept of the relative vorticity gradient acting like the planetary vorticity gradient. Interestingly, because larger vorticity or vorticity gradient regions are associated with larger geostrophic *EKE* regions, IEB decreases linearly with $\log_{10}$ *EKE*.

[71] We are inclined to think that our observations are most compatible with the results of *Danioux et al.* [2008]. However, a restriction of the applicability of their results here is their requirement that the eddy field is essentially barotropic, i.e., that there is a separation of scale in the vertical between the two types of motions. Mesoscale sea level anomalies that are measured by altimetry represent mostly the first baroclinic mode [*Wunsch*, 1997]. In contrast, NIOs are supposedly excited within the mixed layer and vertically uniform. Thus, the vertical extension of the geostrophic vorticity is expected to be greater that the vertical extension of NIOs captured by surface drifter, which are drogued to follow the water at a depth of 15 m. Note, however, that *Danioux et al.* [2008] considered the free decay of NIOs and that drifter observations are in the perpetually forced real ocean.

[72] Our observations can also be compared to the ideas of *Polzin* [2008], who investigated mesoscale eddy internal wave coupling from vertical profiles of horizontal velocity in the MODE experiment. He concluded that those data were consistent with internal wave dynamics affected dominantly by Doppler shifting and a wave capture scenario [*Bühler and McIntyre*, 2005]. Here, the magnitude of the geostrophic strain, as estimated by the altimetry data set, is strongly correlated with the geostrophic *EKE* (not shown). Therefore, the influence of the strain on the characteristics of NIOs is very similar to *EKE*, that is while RFS and NIV are mostly independent of the strain, IEB decreases strongly with increasing strain. However, the applicability of the wave capture scenario to our observations is unclear.

[73] The modification of NIOs by the mesoscale is of course a time-dependent problem, so that the implicit assumption of stationarity made in our analysis of the drifter velocity spectrum is not always true. However, the compatibility of our observations with analytical and numerical predictions suggest that these theories may at least partly apply to the real ocean. If so, our results reinforce the idea that the vertical propagation of inertial energy from a source at the surface like the wind is strongly conditioned by the mesoscale field, especially the asymmetric modification of cyclonic and anticyclonic vorticity. Oceanic general circulation models should take these effects explicitly into account in their vertical mixing scheme near the suface [e.g., *Zhai et al.*, 2009, and references therein].

[74] **Acknowledgments.** Shane Elipot was partially supported by the Cooperative Institute for Marine and Atmospheric Studies, by the UK Natural Environment Research Council as a contribution to Oceans 2025, and by the UK National Centre for Earth Observation. Rick Lumpkin was supported by NOAA's Office of Climate Observations and AOML. The authors would like to thank Mayra Pazos, Jessica Redman, and Erik Valdez of the GDP Data Assembly Center, who prepared the quality-controlled data set. The authors would like to thank Jonathan Lilly for useful conversations, Patrice Klein for his comments on the manuscript, and two anonymous reviewers for constructive criticisms. The author would also like to thank Lana Erofeeva for her assistance for running the OSU TPXO tidal model.

References

Alford, M. H. (2003), Redistribution of energy available for ocean mixing by long-range propagation of internal waves, *Nature*, *423*(6936), 159–162.

Alford, M. H., and M. Whitmont (2007), Seasonal and spatial variability of near-inertial kinetic energy from historical moored velocity records, *J. Phys. Oceangr.*, *37*(8), 2022–2037.

Bühler, O., and M. McIntyre (2005), Wave capture and wave-vortex duality, *J. Fluid Mech.*, *534*, 67–95.

Chaigneau, A., O. Pizarro, and W. Rojas (2008), Global climatology of near-inertial current characteristics from Lagrangian observations, *Geophys. Res. Lett.*, *35*, L13603, doi:10.1029/2008GL034060.

Danioux, E., P. Klein, and P. Rivière (2008), Propagation of wind energy into the deep ocean through a fully turbulent mesoscale eddy field, *J. Phys. Oceanogr.*, *38*(10), 2322–2329.

D'Asaro, E. (1995), Upper-ocean inertial currents forced by a strong storm. Part III: Interaction of inertial currents and mesoscale eddies, *J. Phys. Oceanogr.*, *25*(11), 2953–2958.

de Boyer Montegut, C., J. Mignot, A. Lazar, and S. Cravatte (2007), Control of salinity on the mixed layer depth in the world ocean. Part I: General description, *J. Geophys. Res.*, *107*, C06011, doi:10.1029/2006JC003953.

Ducet, N., P. Y. Le Traon, and G. Reverdin (2000), Global high-resolution mapping of ocean circulation from TOPEX/Poseidon and ERS-1 and-2, *J. Geophys. Res.*, *105*(C8), 19,477–19,498.

Egbert, G. D., and S. Y. Erofeeva (2002), Efficient inverse modeling of barotropic ocean tides, *J. Atmos. Oceanic Technol.*, *19*(2), 183–204.

Elipot, S., and R. Lumpkin (2008), Spectral description of oceanic near-surface variability, *Geophys. Res. Lett.*, *35*, L05606, doi:10.1029/2007GL032874.

Flierl, G. R. (1978), Models of vertical structure and the calibration of two-layer models, *Dyn. Atmos. Oceans*, *2*, 341–381.

Fu, L.-L. (1981), Observations and models of inertial waves in the deep ocean, *Rev. Geosphys. Space Phys.*, *19*, 141–170.

Garrett, C. (2001), What is the "near-inertial" band and why is it different from the rest of the internal wave spectrum?, *J. Phys. Oceanogr.*, *31*(4), 962–971.

Gill, A. E. (1984), On the behavior of internal waves in the wakes of storms, *J. Phys. Oceanogr.*, *14*(7), 1129–1151.

Gonella, J. (1972), A rotary-component method for analysing meteorological and oceanographic vector time series, *Deep Sea Res.*, *19*(12), 833–846.

Hansen, D. V., and P.-M. Poulain (1996), Quality control and interpolations of WOCE-TOGA drifter data, *J. Atmos. Oceanic Technol.*, *13*(4), 900–909.

Hughes, C. W., A. F. Thompson, and C. Wilson (2009), Identification of jets and mixing barriers from sea level and vorticity measurements using simple statistics, *Ocean Modell.*, *32*, 44–57, doi:10.1016/j.ocemod.2009.10.004.

Klein, P., and S. Llewellyn-Smith (2001), Horizontal dispersion of near-inertial oscillations in a turbulent mesoscale eddy field, *J. Mar. Res.*, *59*(5), 697–723.

Klein, P., G. Lapeyre, and W. G. Large (2004a), Wind ringing of the ocean in presence of mesoscale eddies, *Geophys. Res. Lett.*, *31*, L15306, doi:10.1029/2004GL020274.

Klein, P., S. Smith, and G. Lapeyre (2004b), Organization of near-inertial energy by an eddy field, *Q. J. R. Meteorol. Soc.*, *130*, 1153–1166.

Klein, P., B. Hua, G. Lapeyre, X. Capet, S. Le Gentil, and H. Sasaki (2008), Upper ocean turbulence from high-resolution 3D simulations, *J. Phys. Oceanogr.*, *38*(8), 1748–1763.

Kunze, E. (1985), Near-inertial wave propagation in geostrophic shear, *J. Phys. Oceanogr.*, *15*(5), 544–565.

Kunze, E., and T. Sanford (1984), Observations of near-inertial waves in a front, *J. Phys. Oceanogr.*, *14*(3), 566–581.

Lilly, J. M., and S. C. Olhede (2009), Bivariate instantaneous frequency and bandwidth, *IEEE Trans. Signal Process.*, *58*, 591–603.

Lumpkin, R., and M. Pazos (2007), Measuring surface currents with SVP drifters: The instrument, its data, and some recent results, in *Lagrangian Analysis and Prediction of Coastal and Ocean Dynamics*, edited by A. Griffa et al., pp. 39–67, Cambridge Univ. Press, Cambridge, U. K.

Lumpkin, R., A. Treguier, and K. Speer (2002), Lagrangian eddy scales in the northern Atlantic Ocean, *J. Phys. Oceanogr.*, *32*(9), 2425–2440.

Maximenko, N., and P. Niiler (2006), Mean surface circulation of the global ocean inferred from satellite altimeter and drifter data, in *15 Years of Progress in Radar Altimetry*, *Publ. SP-614*, Eur. Space Agency, Paris.

Middleton, J. F., and C. Garrett (1986), A kinematic analysis of polarized eddy fields using drifter data, *J. Geophys. Res.*, *91*(C4), 5094–5102.

Park, J. J., K. Kim, and B. A. King (2005), Global statistics of inertial motions, *Geophys. Res. Lett.*, *32*, L14612, doi:10.1029/2005GL023258.

Park, J. J., K. Kim, and R. W. Schmitt (2009), Global distribution of the decay timescale of mixed layer inertial motions observed by satellite-tracked drifters, *J. Geophys. Res.*, *114*, C11010, doi:10.1029/2008JC005216.

Plueddemann, A. J., and J. T. Farrar (2006), Observations and models of the energy flux from the wind to mixed-layer inertial currents, *Deep Sea Res.*, *53*(1–2), 5–30.

Pollard, R. T., and R. C. J. Millard (1970), Comparison between observed and simulated wind-generated inertial oscillations, *Deep Sea Res.*, *17*(4), 813–821.

Polzin, K. (2008), Mesoscale eddy–internal wave coupling. Part I: Symmetry, wave capture and results from the mid-ocean dynamics experiment, *J. Phys. Oceanogr.*, *38*(11), 2556–2574.

Poulain, P.-M., D. S. Luther, and W. C. Patzert (1992), Deriving inertial wave characteristics from surface drifter velocities: Frequency variability in the Tropical Pacific, *J. Geophys. Res.*, *97*(C11), 17,947–17,959.

Prieto, G. A., R. L. Parker, D. J. Thomson, F. L. Vernon, and R. L. Graham (2007), Reducing the bias of multitaper spectrum estimates, *Geophys. J. Int.*, *171*(3), 1269–1281.

Rainville, L., and R. Pinkel (2004), Observations of energetic high-wavenumber internal waves in the Kuroshio, *J. Phys. Oceanogr.*, *34*(7), 1495–1505, doi:10.1175/1520-0485(2004)034<1495:OOEHIW>2.0.CO;2.

Rio, M. H., and F. Hernandez (2004), A mean dynamic topography computed over the world ocean from altimetry, in situ measurements, and a geoid model, *J. Geophys. Res.*, *109*, C12032, doi:10.1029/2003JC002226.

Shcherbina, A., L. Talley, E. Firing, and P. Hacker (2003), Near-surface frontal zone trapping and deep upward propagation of internal wave energy in the Japan/East Sea, *J. Phys. Oceanogr.*, *33*(4), 900–912.

Simmons, H., R. Hallberg, and B. Arbic (2004), Internal wave generation in a global baroclinic tide model, *Deep Sea Res.*, *51*(25–26), 3043–3068, doi:10.1016/j.dsr2.2004.09.015.

Stammer, D. (1997), Global characteristics of ocean variability estimated from regional TOPEX/Poseidon altimeter measurements, *J. Phys. Oceanogr.*, *27*(8), 1743–1769.

Thomson, D. (1982), Spectrum estimation and harmonic analysis, *Proc. IEEE*, *70*(9), 1055–1096.

van Haren, H. (2004), Bandwidth similarity at inertial and tidal frequencies in kinetic energy spectra from the Bay of Biscay, *Deep Sea Res.*, *51*(5), 637–652, doi:10.1016/j.dsr.2004.01.006.

van Meurs, P. (1998), Interactions between near-inertial mixed layer currents and the mesoscale: The importance of spatial variabilities in the vorticity field, *J. Phys. Oceanogr.*, *28*(7), 1363–1388, doi:10.1175/1520-0485(1998)028<1363:IBNIML>2.0.CO;2.

Wunsch, C. (1997), The vertical partition of oceanic horizontal kinetic energy, *J. Phys. Oceanogr.*, *27*(8), 1770–1794.

Young, W. R., and M. Ben Jelloul (1997), Propagation of near-inertial oscillations through a geostrophic flow, *J. Mar. Res.*, *55*(4), 735–766.

Zhai, X., R. J. Greatbatch, C. Eden, and T. Hibiya (2009), On the loss of wind-induced near-inertial energy to turbulent mixing in the upper ocean, *J. Phys. Oceanogr.*, *39*(11), 3040–3045, doi:10.1175/2009JPO4259.1.

Zhurbas, V., and I. S. Oh (2003), Lateral diffusivity and Lagrangian scales in the Pacific Ocean as derived from drifter data, *J. Geophys. Res.*, *108*(C5), 3141, doi:10.1029/2002JC001596.

S. Elipot, National Oceanography Centre, 6 Brownlow St., Joseph Proudman Bldg., Liverpool L3 5DA, UK. (ship@pol.ac.uk)

R. Lumpkin, NOAA Atlantic Oceanographic and Meteorological Laboratory, 4301 Rickenbacker Cswy., Miami, FL 33149, USA.

G. Prieto, Departamento de Física, Universidad de los Andes, Calle 18A 1–10 Bloque H, Of. Ñ f204, Bogota AA 4976, Colombia.